Higgs-boson-pair production $H(\to b\bar{b})H(\to \gamma\gamma)$ from gluon fusion at the HL-LHC and HL-100 TeV hadron collider

Jung Chang,[1,2] Kingman Cheung,[2,3,4] Jae Sik Lee,[1,2,5] Chih-Ting Lu,[4] and Jubin Park[5,1,2]

[1]*Department of Physics, Chonnam National University, 300 Yongbong-dong, Buk-gu, Gwangju, 500-757, Republic of Korea*
[2]*Physics Division, National Center for Theoretical Sciences, Hsinchu 300, Taiwan*
[3]*Division of Quantum Phases and Devices, School of Physics, Konkuk University, Seoul 143-701, Republic of Korea*
[4]*Department of Physics, National Tsing Hua University, Hsinchu 300, Taiwan*
[5]*Institute for Universe and Elementary Particles, Chonnam National University, 300 Yongbong-dong, Buk-gu, Gwangju, 500-757, Republic of Korea*

(Received 19 June 2018; revised manuscript received 31 July 2018; published 4 November 2019)

We perform the most up-to-date comprehensive signal-background analysis for Higgs-pair production in $HH \to b\bar{b}\gamma\gamma$ channel at the HL-LHC and HL-100 TeV hadron collider, with the goal of probing the self-coupling λ_{3H} of the Higgs boson which is normalized to its standard-model value of 1. We simulate all the standard-model signal and background processes and emphasize that the $ggH(\to \gamma\gamma)$ background has been overlooked in previous studies. We find that, even for the most promising channel $HH \to b\bar{b}\gamma\gamma$ at the HL-LHC with a luminosity of 3000 fb^{-1}, the significance is still not high enough to establish the Higgs self-coupling at the standard-model (SM) value. Instead, we can only constrain the self-coupling to $-1.0 < \lambda_{3H} < 7.6$ at 95% confidence level after considering the uncertainties associated with the top-Yukawa coupling and the estimation of backgrounds. Here we also extend the study to the HL-100 TeV hadron collider. With a luminosity of 3 ab^{-1}, we find there exists a bulk region of $2.6 \lesssim \lambda_{3H} \lesssim 4.8$ in which one cannot pin down the trilinear coupling. Otherwise, one can measure the coupling with a high precision. At the SM value, for example, we show that the coupling can be measured with about 20% accuracy. While assuming 30 ab^{-1}, the bulk region reduces to $3.1 \lesssim \lambda_{3H} \lesssim 4.3$, and the trilinear coupling can be measured with about 7% accuracy at the SM value.

DOI: 10.1103/PhysRevD.100.096001

I. INTRODUCTION

The origin of mass is the most important question that one would ask for our existence. This is related to the mechanism involved in electroweak symmetry breaking (EWSB), which is believed to give masses to gauge bosons and fermions. The simplest implementation in our standard model (SM) is to introduce a Higgs doublet field, whose nonvanishing vacuum expectation value causes EWSB [1]. The by-product is a neutral scalar Higgs boson, which was eventually discovered in July 2012 [2]. After accumulating enough data at the end of 8 TeV runs, the scalar boson is best described by the SM Higgs boson [3], in which the couplings to gauge bosons are firmly established and those to fermions started to fall in the ballpark of the SM values. However, the SM Higgs boson can hardly constitute a complete theory because of, for example, the gauge hierarchy problem.

The current measurements of the Higgs-boson properties mainly concern the couplings of the Higgs boson to the SM particles. There is no *a priori* reason why the EWSB sector simply contains only one Higgs doublet field. Indeed, many extensions of the EWSB sector consist of more Higgs fields. Until now, there is no information at all about the self-couplings of the Higgs boson, which depends on the dynamics of the EWSB sector. The self-couplings of the Higgs boson are very different among the SM, two-Higgs doublet models, and minimal supersymmetric extension of the standard model. One of the probes of Higgs self-coupling is Higgs-boson-pair production at the LHC [4–6]. There have been a large number of works in the literature on Higgs-pair production in the SM [7], in model-independent formalism [8], in models beyond the SM [9], and in supersymmetry [10].

The predictions for various models are largely different such that the production rates can give valuable information on the self-coupling λ_{3H}. In the SM, Higgs-pair production

receives contributions from both the triangle and box diagrams, which interfere with each other. It is only the triangle diagram that involves the Higgs self-trilinear coupling λ_{3H}, yet the top-Yukawa coupling appears in both triangle and box diagrams. Therefore, we have to disentangle the triangle diagram from the box diagram in order to probe the Higgs trilinear coupling. In Ref. [11], we pointed out that the triangle diagram, with an s-channel Higgs propagator, is more important at a low invariant-mass region than the box diagram. Thus, the Higgs-boson pair from the triangle diagram tends to have a lower invariant mass, and, therefore, the opening angle in the decay products of each Higgs boson tends to be larger than that from the box diagram. Indeed, the opening angle separations $\Delta R_{\gamma\gamma}$ and ΔR_{bb} between the decay products of the Higgs-boson pair are very useful variables to disentangle the two sources. However, in Ref. [11] we assumed only some level of signal uncertainties to evaluate the sensitivity to the parameter space of self-coupling λ_{3H} and the top-Yukawa coupling g_t^S, without calculating all the other SM backgrounds, e.g., jet-fake backgrounds, single-Higgs associated backgrounds, and nonresonant backgrounds.

In this work, we perform the most up-to-date comprehensive signal-background analysis for Higgs-pair production through gluon fusion and the $HH \to b\bar{b}\gamma\gamma$ decay channel. For other production and decay channels and some combined analyses, see Ref. [12]. We simulate the signal and all background processes using simulation tools as sophisticated as what experimentalists use. The signal subprocess is $gg \to HH \to b\bar{b}\gamma\gamma$ with various values for λ_{3H}. The background includes $t\bar{t}$, $t\bar{t}\gamma$, single-Higgs associated backgrounds (e.g., ZH, $t\bar{t}H$, $b\bar{b}H$, ggH followed by $H \to \gamma\gamma$), and nonresonant or jet-fake backgrounds (e.g., $b\bar{b}\gamma\gamma$, $b\bar{b}j\gamma$, $b\bar{b}jj$, $jj\gamma\gamma$, etc). We found a set of useful selection cuts to reduce the backgrounds. We express the sensitivity that can be achieved in terms of significance. We find that, even for the most promising channel $HH \to b\bar{b}\gamma\gamma$ at the HL-LHC, the significance is still not high enough to establish the Higgs self-coupling at the SM value, though the self-coupling can be constrained to the range $0 < \lambda_{3H} < 7.1$ at 95% confidence level (C.L.) with an integrated luminosity of 3000 fb^{-1}. Taking account of the uncertainties associated with the top-Yukawa coupling and the estimation of backgrounds, we have found that the 95% C.L. region broadens into $-1.0 < \lambda_{3H} < 7.6$. We also extend the analysis to the HL-100 TeV hadron collider. With a luminosity of 3 ab^{-1}, we find a bulk region of $2.6 \lesssim \lambda_{3H} \lesssim 4.8$ in which one cannot pin down the trilinear coupling. Otherwise, one can measure the coupling with a high precision. At the SM value, for example, we show that the coupling can be measured with about 20% accuracy. While assuming 30 ab^{-1}, the bulk region reduces to $3.1 \lesssim \lambda_{3H} \lesssim 4.3$, and the trilinear coupling can be measured with about 7% accuracy at the SM value. This is the main result of this work.

This work has a number of improvements over our previous and other works in the literature, summarized as follows.

(1) We have included all the backgrounds, including $t\bar{t}$-related ones, single-Higgs associated production processes, nonresonant backgrounds, and jet-fake backgrounds. Furthermore, we emphasize that we have implemented through detector simulations of all the backgrounds.
(2) While implementing all the relevant signal and background simulations, we find that the $ggH(\to\gamma\gamma)$ background is possibly very important and has been overlooked in previous studies. Note that a similar observation has been recently made by the authors of Ref. [13].
(3) For the signal, since the signal distributions behave differently for different λ_{3H}, we evaluate the selection efficiency separately for each λ_{3H} to properly cover the viable range of the nonstandard values of λ_{3H}.
(4) At the HL-LHC, we first take into account the impact of the uncertainty associated with the top-Yukawa coupling on 95% C.L. sensitivity. We find that, especially, the lower boundary of the 95% C.L. region of λ_{3H} significantly varies upon the expected precision of the top-quark Yukawa coupling in the HL-LHC era.
(5) Taking account of all the backgrounds known up to date and devising a *new* set of selection cuts, we have most reliably estimated the potential reach of the HL-100 TeV hadron collider for a broad range of λ_{3H}.
(6) At the HL-100 TeV collider, we find there is a twofold ambiguity in λ_{3H} which could be lifted up by exploiting several kinematical distributions. We also find that there exists a bulk region in which it would be difficult to establish the λ_{3H} coupling even at the HL-100 TeV collider.

The organization is as follows. In the next section, we briefly describe the effective Lagrangian for Higgs-pair production. In Sec. III, we describe the signal and background processes and simulation tools. We also present the distributions, selection cuts, cut flows of signal and backgrounds, and significance for the HL-LHC. Section IV is dedicated to the case of the HL-100 TeV hadron collider. In Sec. V, we examine the impact of the next-to-leading-order (NLO) corrections considering full top-quark mass dependence, the effect of using a modern parton distribution function (PDF) set to include the LHC data on the PDF, and how the investigation of the uncertainties involved in the matching procedures affects the 95% C.L. sensitivity region of λ_{3H}. We discuss and conclude in Sec. VI. We put some extra distributions and cut flow tables, which can be ignored in the first reading, into Appendixes A and B. Appendix C, on the other hand, gives the details for the

procedures employed in the matching in calculating the cross sections of the nonresonant backgrounds, as well as their uncertainties.

II. EFFECTIVE LAGRANGIAN

The contributing Feynman diagrams for Higgs-boson-pair production via gluon fusion include a triangle diagram with a Higgs-boson propagator and a box diagram with colored particles running in them. The relevant couplings involved are top-Yukawa and the Higgs trilinear self-coupling, which are given in this Lagrangian:

$$-\mathcal{L} = \frac{1}{3!}\left(\frac{3M_H^2}{v}\right)\lambda_{3H}H^3 + g_t^S\frac{m_t}{v}\bar{t}tH. \tag{1}$$

In the SM, $\lambda_{3H} = g_t^S = 1$. The differential cross section for the process $g(p_1)g(p_2) \to H(p_3)H(p_4)$ was obtained in Ref. [14] as

$$\frac{d\hat{\sigma}(gg \to HH)}{d\hat{t}} = \frac{G_F^2\alpha_s^2}{512(2\pi)^3}[|\lambda_{3H}g_t^S D(\hat{s})F_\Delta^S + (g_t^S)^2F_\square^{SS}|^2 + |(g_t^S)^2G_\square^{SS}|^2], \tag{2}$$

where

$$D(\hat{s}) = \frac{3M_H^2}{\hat{s} - M_H^2 + iM_H\Gamma_H} \tag{3}$$

$\hat{s} = (p_1 + p_2)^2$, $\hat{t} = (p_1 - p_3)^2$, and $\hat{u} = (p_2 - p_3)^2$ with $p_1 + p_2 = p_3 + p_4$. The loop functions $F_\Delta^S = F_\Delta$, $F_\square^{SS} = F_\square$, and $G_\square^{SS} = G_\square$ with $F_{\triangle,\square}$ and $G_\square$ are given in Appendix A.1 in Ref. [14]. In the heavy quark limit, one may have

$$F_\Delta^S = +\frac{2}{3} + \mathcal{O}(\hat{s}/m_Q^2), \qquad F_\square^{SS} = -\frac{2}{3} + \mathcal{O}(\hat{s}/m_Q^2), \qquad G_\square^{SS} = \mathcal{O}(\hat{s}/m_Q^2), \tag{4}$$

leading to a large cancellation between the triangle and box diagrams.

The production cross section normalized to the corresponding SM cross section, with or without cuts, can be parameterized as follows:

$$\frac{\sigma^{\rm LO}(gg \to HH)}{\sigma^{\rm LO}_{\rm SM}(gg \to HH)} = c_1(s)\lambda_{3H}^2(g_t^S)^2 + c_2(s)\lambda_{3H}(g_t^S)^3 + c_3(s)(g_t^S)^4, \tag{5}$$

where the numerical coefficients $c_{1,2,3}(s)$ depend on s and experimental selection cuts. Numerically, $c_1(s)$, $c_2(s)$, and $c_3(s)$ are 0.263, −1.310, and 2.047, respectively, at 14 TeV and 0.208, −1.108, and 1.900, respectively, at 100 TeV [11]. Upon our normalization, the ratio should be equal to 1 when $g_t^S = \lambda_{3H} = 1$, or $c_1(s) + c_2(s) + c_3(s) = 1$. The coefficients $c_1(s)$ and $c_3(s)$ are for the contributions from the triangle and box diagrams, respectively, and the coefficient $c_2(s)$ for the interference between them. Once we have the coefficients c_i, the cross sections can be easily obtained for any combination of couplings.

To get a feeling for the size of the cross sections that we are considering, we show the total production cross sections for various HH production channels in Fig. 1. At 14 TeV, the SM cross sections $\sigma(gg \to HH) = 45.05$ fb [15], $\sigma(qq' \to HHqq') = 1.94$ fb [16], $\sigma(q\bar{q}(') \to VHH = 0.567(V = W^\pm)/0.415(V = Z)$ fb [17], and $\sigma(gg/q\bar{q} \to t\bar{t}HH) = 0.949$ fb [16] are calculated at NNLO + NNLL, NLO, NNLO, and NLO, respectively [18]. The 100 TeV cross sections $\sigma(gg \to HH) = 1749$ fb, $\sigma(qq' \to HHqq') = 80.3$ fb, $\sigma(q\bar{q}(') \to VHH = 8.00(V = W^\pm)/8.23(V = Z)$ fb, and $\sigma(gg/q\bar{q} \to t\bar{t}HH) = 82.1$ fb are calculated at the same orders as at 14 TeV [19,20]. From Fig. 1, it is clear that the gluon fusion into HH gives the largest cross sections independently of λ_{3H} with its minimum occurring at $\lambda_{3H} \simeq 2.5$. From now on, we shall focus on the gluon fusion mechanism. We show the ratio of the cross sections for the $gg \to HH$ process as a function of λ_{3H} in Fig. 2, in

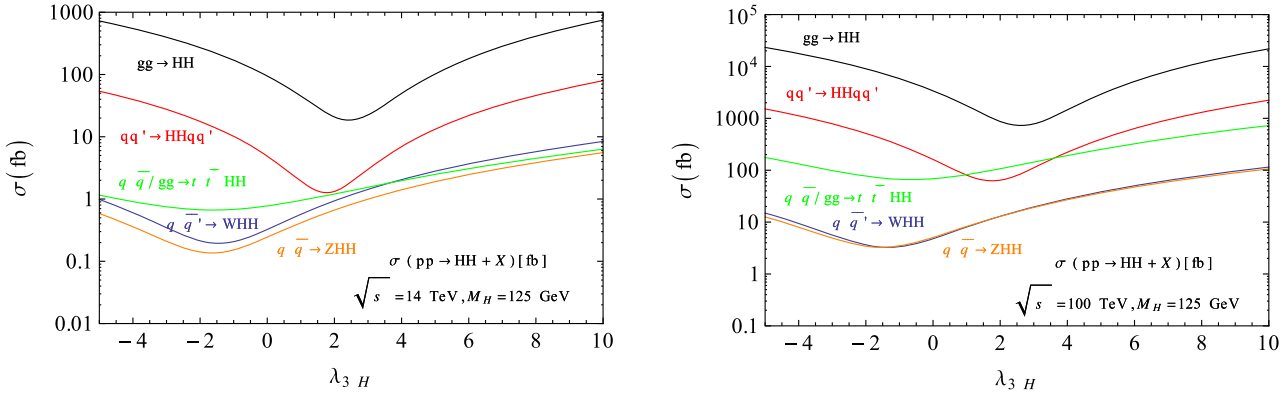

FIG. 1. Production cross sections for various channels for HH production at $\sqrt{s} = 14$ TeV (left) and $\sqrt{s} = 100$ TeV (right). The NNPDF2.3LO PDF set is used.

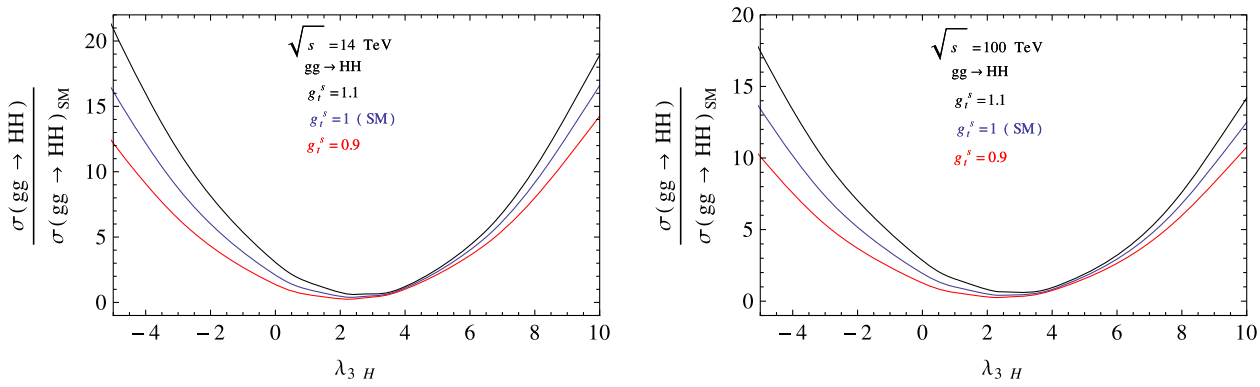

FIG. 2. Ratio of cross sections $\sigma(gg \to HH)/\sigma(gg \to HH)_{\rm SM}$ versus λ_{3H} taking account of 10% uncertainty of the top-Yukawa coupling: $g_t^S = 1.1$ (black curve), 1 (blue curve), and 0.9 (red curve) for $\sqrt{s} = 14$ TeV (left) and $\sqrt{s} = 100$ TeV (right).

which we also indicate the effects of allowing the top-Yukawa coupling to have $\pm 10\%$ uncertainty or $\delta g_t^S = \pm 0.1$. At the HL-LHC, the expected precision of measurement of the top-quark Yukawa coupling is 10% [21]. Currently, without knowing the absolute value of the top-quark Yukawa coupling no better than 10% precision, we also consider the $\delta g_t^S = \pm 10\%$ effect at 100 TeV though the expected uncertainty is 1% at the 100 TeV pp colliders.

III. SIMULATIONS, EVENT SELECTIONS, AND ANALYSIS AT THE 14 TEV HL-LHC

Our goal is to disentangle the effects of trilinear Higgs coupling, which is present in the triangle diagram, in Higgs-pair production. We focus on the decay channel $HH \to b\bar{b}\gamma\gamma$, in which the final state consists of a pair of b quarks and a pair of photons reconstructed at the invariant mass around the Higgs-boson mass ($M_H \simeq 125$ GeV). We shall vary the value for the trilinear coupling λ_{3H} between -5 and 10 to visualize the effects of λ_{3H}. The backgrounds then include

(i) single-Higgs associated production, such as ggH, $t\bar{t}H$, ZH, $b\bar{b}H$ followed by $H \to \gamma\gamma$,
(ii) nonresonant backgrounds and jet-fake backgrounds, such as $b\bar{b}\gamma\gamma$, $c\bar{c}\gamma\gamma$, $jj\gamma\gamma$, $b\bar{b}j\gamma$, $c\bar{c}j\gamma$, $b\bar{b}jj$, and $Z\gamma\gamma \to b\bar{b}\gamma\gamma$, and
(iii) $t\bar{t}(\geq 1$ lepton) and $t\bar{t}\gamma(\geq 1$ lepton) backgrounds.

All the signal and backgrounds are summarized in Table I, together with the information of the corresponding event generator, the cross section times the branching ratio ($\sigma \cdot$ BR), the order in QCD for the calculation of $\sigma \cdot$ BR, and the PDF used.

A. Parton-level event generations and detector simulations

Parton-level events for the backgrounds [$b\bar{b}\gamma\gamma$, $c\bar{c}\gamma\gamma$, $jj\gamma\gamma$, $b\bar{b}j\gamma$, $c\bar{c}j\gamma$, $b\bar{b}jj$, $t\bar{t}\gamma$, and $Z(\to b\bar{b})\gamma\gamma$] and for the signal (with $-5 \leq \lambda_{3H} \leq 10$) are generated with MADGRAPH5_AMC@NLO (MG5_aMC@NLO) [24]. Backgrounds for gluon fusion and top-quark pair are generated with POWHEG BOX [25]. The single-Higgs associated backgrounds for $t\bar{t}H(\to\gamma\gamma)$, $ZH(\to\gamma\gamma)$, and $b\bar{b}H(\to\gamma\gamma)$ are generated with PYTHIA8 [26]. Here we would like to provide more detailed information on the parton-level generation of signal and background events. The signal cross sections are calculated with the adjustable Higgs self-coupling in universal FeynRules output format [27] and events are generated in the loop-induced mode [28]. The MADSPIN code [29] is then employed to let the Higgs-boson pair decay into $b\bar{b}\gamma\gamma$. Further on the parton-level generation of nonresonant and $t\bar{t}\gamma$ backgrounds, the following preselection cuts at the parton level are imposed in order to avoid any divergence in the parton-level calculations [30]:

$$\begin{aligned} &P_{T_j} > 20\,\text{GeV}, \quad P_{T_b} > 20\,\text{GeV}, \\ &P_{T_\gamma} > 25\,\text{GeV}, \quad P_{T_l} > 10\,\text{GeV}, \\ &|\eta_j| < 5, \quad |\eta_\gamma| < 2.7, \quad |\eta_l| < 2.5, \\ &\Delta R_{jj,ll,\gamma\gamma,\gamma j,jl,\gamma l} > 0.4, \quad M_{jj} > 25\,\text{GeV}, \\ &M_{bb} > 45\,\text{GeV}, \quad 60 < M_{\gamma\gamma} < 200\,\text{GeV}. \end{aligned} \tag{6}$$

For parton showering, hadronization, and decays of unstable particles, PYTHIA8 [26] is used for both signal and backgrounds. Finally, fast detector simulation and analysis at the HL-LHC are performed using DELPHES3 [31] with the ATLAS template. In the template, we use the expected performance for photon efficiency, photon fake rates, b-jet tagging efficiency, and b-jet fake rates obtained with a mean pileup $\langle\mu\rangle = 200$ (see Refs. [30,32]). For the photon efficiency, we use the P_T-dependent formula

$$\epsilon_\gamma = 0.888 * \tanh(0.01275 * P_{T_\gamma}/\text{GeV}),$$

which we obtain by fitting to the ATLAS simulation results. At $P_{T_\gamma} \sim 50$ GeV, $\epsilon_\gamma \sim 50\%$ as in Ref. [30] and it approaches $\epsilon_\gamma \sim 85\%$ in the saturation region of the curve, at $P_{T_\gamma} \sim 150$ GeV to be specific, being consistent with the ATLAS simulation [32]. The photon fake rates are

TABLE I. Monte Carlo samples used in Higgs-pair production analysis $H(\to b\bar{b})H(\to\gamma\gamma)$ and the corresponding codes for the matrix-element generation, parton showering, and hadronization. The third (fourth) column shows their cross section times branching ratio (the order in perturbative QCD of the cross section calculation applied), and the final column shows their PDF set used in the simulation. For the generation of nonresonant and $t\bar{t}\gamma$ backgrounds, some preselection cuts are applied at the parton level in order to remove the divergence associated with the photons or jets; see Eq. (6). Note that, except the $ggH(\to\gamma\gamma)$ and $t\bar{t}$ backgrounds which are generated at NLO, all the signal and backgrounds are generated at LO and normalized to the cross sections computed at the accuracy denoted in "Order in QCD."

Signal				
Signal process	Generator/parton shower	$\sigma \cdot$ BR [fb]	Order in QCD	PDF used
$gg \to HH \to b\bar{b}\gamma\gamma$ [18]	MG5_aMC@NLO/PYTHIA8	0.119	NNLO + NNLL	NNPDF2.3LO

Backgrounds					
Background (BG)	Process	Generator/parton shower	$\sigma \cdot$ BR [fb]	Order in QCD	PDF used
Single-Higgs associated BG [18]	$ggH(\to\gamma\gamma)$	POWHEG BOX/PYTHIA6	1.20×10^2	NNNLO	CT10
	$t\bar{t}H(\to\gamma\gamma)$	PYTHIA8/PYTHIA8	1.37	NLO	
	$ZH(\to\gamma\gamma)$	PYTHIA8/PYTHIA8	2.24	NLO	
	$b\bar{b}H(\to\gamma\gamma)$	PYTHIA8/PYTHIA8	1.26	NLO	
Nonresonant BG	$b\bar{b}\gamma\gamma$	MG5_aMC@NLO/PYTHIA8	1.40×10^2	LO	CTEQ6L1
	$c\bar{c}\gamma\gamma$	MG5_aMC@NLO/PYTHIA8	1.14×10^3	LO	
	$jj\gamma\gamma$	MG5_aMC@NLO/PYTHIA8	1.62×10^4	LO	
	$b\bar{b}j\gamma$	MG5_aMC@NLO/PYTHIA8	3.67×10^5	LO	
	$c\bar{c}j\gamma$	MG5_aMC@NLO/PYTHIA8	1.05×10^6	LO	
	$b\bar{b}jj$	MG5_aMC@NLO/PYTHIA8	4.34×10^8	LO	
	$Z(\to b\bar{b})\gamma\gamma$	MG5_aMC@NLO/PYTHIA8	5.17	LO	
$t\bar{t}$ and $t\bar{t}\gamma$ BG ($\geq$1 lepton)	$t\bar{t}$ [22]	POWHEG BOX/PYTHIA8	5.30×10^5	NNLO + NNLL	CT10
	$t\bar{t}\gamma$ [23]	MG5_aMC@NLO/PYTHIA8	1.60×10^3	NLO	CTEQ6L1

taken from Ref. [30]: $P_{j\to\gamma} = 5\times10^{-4}$ and $P_{e\to\gamma} = 2\%(5\%)$ in the barrel (end cap) region. The b-jet tagging efficiency ϵ_b depends on P_T and η of the b jet, and we have fully considered its P_T and η dependence; see Fig. 7(b) in Ref. [32]. The charm-jet fake rate $P_{c\to b}$ depends on ϵ_b and, accordingly, on P_T and η of the c jet. For the multivariate MV1 b-tagging algorithm taken in our analysis, $P_{c\to b} \sim 1/5$ when $\epsilon_b = 0.7$, and it approaches 1 as $\epsilon_b \to 1$ [33]. In our simulation, the P_T and η dependence of $P_{c\to b}$ is also considered. For the light-jet fake rate, we are taking $P_{j\to b} = 1/1300$ [30]. Incidentally, we have also considered the energy loss due to the b momentum reconstruction from the b-tagged jet and set the jet-energy scale using the scaling formula [31]

$$\sqrt{\frac{(3.0 - 0.2|\eta_b|)^2}{P_{T_b}/\mathrm{GeV}} + 1.27},$$

where the factor 1.27 is tuned to get a correct peak position at M_H in the invariant mass distribution of a b-quark pair in the signal process.

In this study, we do not include the pileup effects in our simulation. There are a couple of reasons for this. First, it is expected that the pileup effects can be dealt with by the upgraded event trigger in the future, and its overall effect could be negligible in the channel of our interests.[1] More importantly, by imposing a narrow $M_{\gamma\gamma}$ invariant mass window cut in event selection, we could eventually obtain similar results independently of including the pileup effects. This is because pileup causes a stronger impact on photons than on b jets and the soft fake photons from pileup jets make the width of $M_{\gamma\gamma}$ peak wider. Incidentally, we also have checked that the simulation results using the ATLAS b-tagging efficiency in the presence of pileup are similar to those obtained by using the b-tagging efficiency in the absence of pileup (the MV1 algorithm).

B. Signal event samples

The dominant mechanism for Higgs-pair production is the gluon fusion process at the hadron colliders. Other processes are more than an order of magnitude smaller. Thus, only the gluon fusion production mode is used for the signal process $HH \to b\bar{b}\gamma\gamma$. These samples are generated with MADGRAPH5_AMC@NLO at LO.[2] They are showered by

[1] It is shown that the rejection factor for pileup jets could be 1350 with a mean pileup $\langle\mu\rangle = 200$ [30]. According to the ATLAS simulation, only 0%(1.28%) and 0.54%(4.03%) of jets identified as (sub)leading b jets and reconstructed (sub)leading photons, respectively, originate from pileup jets.

[2] We use $m_t = 172$ GeV.

TABLE II. The production cross section times the branching ratio $\sigma \cdot \mathrm{BR}(HH \to b\bar{b}\gamma\gamma)$ at the 14 TeV LHC.

λ_{3H}	−4	0	1	2	6	10
$\sigma \cdot \mathrm{BR}(HH \to b\bar{b}\gamma\gamma)$ [fb]	1.45	0.25	0.12	0.06	0.48	1.97

PYTHIA8 to model the parton showering and hadronization. Note that the A14 tune and the NNPDF2.3LO PDF [34] set are used together.

The signal event samples are generated with various self-coupling strengths in order to show their characteristics: $-5 \le \lambda_{3H} \le 10$ with $\lambda_{3H} = 1$ corresponding to the SM Higgs self-coupling strength. And, the expected signal yields are normalized to the cross section computed at next-to-next-to-leading-order (NNLO) accuracy including next-to-next-to-leading-log (NNLL) gluon resummation [18].[3] In Table II, we show the production cross section times the branching ratio at the 14 TeV LHC for six selected values of $\lambda_{3H} = -4, 0, 1, 2, 6, 10$. To obtain the production cross section σ for the non-SM values of $\lambda_{3H} \neq 1$, we have used[4]

$$\sigma = \frac{\sigma^{\mathrm{LO}}}{\sigma^{\mathrm{LO}}_{\mathrm{SM}}} \times \sigma^{\mathrm{NNLO+NNLL}}_{\mathrm{SM}}. \tag{7}$$

C. Background samples

The backgrounds mainly come from the processes with multiple jets and photons. They can mimic the signal-like two photons and two b jets in the final state. These backgrounds can be categorized into

(i) *single-Higgs associated backgrounds.*—$ggH(\gamma\gamma)$, $t\bar{t}H(\gamma\gamma)$, $ZH(\gamma\gamma)$, and $b\bar{b}H(\gamma\gamma)$,
(ii) *nonresonant (continuum) backgrounds.*—$b\bar{b}\gamma\gamma$, $c\bar{c}\gamma\gamma$, $jj\gamma\gamma$, $b\bar{b}j\gamma$, $c\bar{c}j\gamma$, $b\bar{b}jj$, and $Z(b\bar{b})\gamma\gamma$ events with an additional jet, and
(iii) $t\bar{t}$ and $t\bar{t}\gamma$ backgrounds in which at least one of the top quarks decays leptonically.

The information is summarized in Table I.

1. Single-Higgs associated backgrounds

The gluon-fusion process $ggH(\gamma\gamma)$ is generated using POWHEG BOX [25], and then the background yield is normalized using the cross section at next-to-next-to-next-leading order (NNNLO) in QCD [18]. The samples for $t\bar{t}H(\gamma\gamma)$, $ZH(\gamma\gamma)$, and $b\bar{b}H(\gamma\gamma)$ are generated using PYTHIA8, and they are normalized to the cross sections calculated at NLO in QCD [18].

2. Nonresonant backgrounds

The nonresonant or continuum background (BG) processes included for the analysis are $b\bar{b}\gamma\gamma$, $c\bar{c}\gamma\gamma$, $jj\gamma\gamma$, $b\bar{b}j\gamma$, $c\bar{c}j\gamma$, $b\bar{b}jj$, and $Z(b\bar{b})\gamma\gamma$. They are all generated with MADGRAPH5_AMC@NLO and interfaced with PYTHIA8 for showering and hadronization, and the CTEQ6L1 PDF [35] set is taken. Note that these samples are generated inclusively with an additional hard jet to capture the bulk of the NLO corrections. We then avoid the double counting problems in our nonresonant background samples by applying the preselection cuts listed in Eq. (6). We have found that the resulting cross sections for the nonresonant backgrounds, presented in Table I, agree with those presented in Ref. [30] within errors of less than 5%.

Among them, as will be shown, the $b\bar{b}\gamma\gamma$ and $b\bar{b}j\gamma$ samples give the dominant BG yields. In the latter, j is faking γ. The subdominant BGs come from the $c\bar{c}\gamma\gamma$, $c\bar{c}j\gamma$, and $b\bar{b}jj$ processes with c faking b and/or j faking γ. And the next subleading BG is from the $jj\gamma\gamma$ sample. Here, one should be cautious about the $jj\gamma\gamma$ process, because it receives contributions not only from the light hard quarks and gluons but also from hard charm quarks. Schematically, one may write[5]

$$\begin{aligned} jj\gamma\gamma &\simeq \sum_{j_h^l, j_h, \mathcal{S}} [1 \oplus j_h^l] \otimes [j_h j_h \gamma\gamma] \otimes [1 \oplus \mathcal{S}] \\ &\simeq \sum_{\{j_h^l\}, \mathcal{S}} \{[1 \oplus j_h^l] \otimes [c_h \bar{c}_h \gamma\gamma] \otimes [1 \oplus \mathcal{S}]\} \\ &\quad \oplus \{[1 \oplus j_h^l] \otimes [j_h^l j_h^l \gamma\gamma] \otimes [1 \oplus \mathcal{S}]\}. \end{aligned} \tag{8}$$

In the first line, j_h^l[6] in the first bracket denotes the additional light hard jet, and $\mathcal{S}$ in the last bracket is for jets generated during the showering process or $\mathcal{S} = j_s^l, j_s^l j_s^l, c_s\bar{c}_s, b_s\bar{b}_s$, etc., with the subscript s standing for showering jets. In the second line, we use $j_h j_h \simeq c_h\bar{c}_h \oplus j_h^l j_h^l$ with the subscript h standing for jets from hard scatterings. We definitely see that the first part of Eq. (8) constitutes a part of the $c\bar{c}\gamma\gamma$ sample and should be removed from the $jj\gamma\gamma$ sample to avoid a double counting. After removing it, we find that the process with $\mathcal{S} = c_s\bar{c}_s$ dominates the $jj\gamma\gamma$ BG with c_s faking b. Note that charm quarks should be treated separately from the light quarks, since the c-quark fake rate $P_{c\to b}$ is much larger than the light-jet fake rate of $P_{j\to b} = 1/1300$. Incidentally, we recall that $P_{j\to\gamma} = 5\times10^{-4}$. Finally, the $Z(b\bar{b})\gamma\gamma$ sample has the least contribution to the nonresonant backgrounds. In Table III, we are summarizing the main fake processes and rates in each sample of backgrounds.

[3]For the signal event normalization, we take the cross section computed in the infinite top-quark mass approximation [18].
[4]See also Fig. 2.
[5]For our $jj\gamma\gamma$ analysis, first we have removed the c jet from a set of an additional hard jet.
[6]Here, j_h^l denotes a light hard jet originating from light u, d, and s quarks and gluons. Do not confuse it with j_h, which is for a hard jet originating not only from the light quarks and gluons but also from c quarks.

TABLE III. The main fake processes and the corresponding rates in each sample of nonresonant and $t\bar{t}(\gamma)$ backgrounds. We recall that $P_{j\to\gamma} = 5\times10^{-4}$ and $P_{e\to\gamma} = 2\%$ (5%) in the barrel (end cap) calorimeter region. For c_s quarks produced during showering in the $jj\gamma\gamma$ sample, we use $P_{c_s\to b} = 1/8$ as in Ref. [30]. Otherwise, the P_T and η dependence of $P_{c\to b}$ is fully considered as explained in the text.

Background (BG)	Process	Fake process	Fake rate
Nonresonant BG	$b\bar{b}\gamma\gamma$	N/A	N/A
	$c\bar{c}\gamma\gamma$	$c\to b$, $\bar{c}\to\bar{b}$	$(P_{c\to b})^2$
	$jj\gamma\gamma$	$c_s\to b$, $\bar{c_s}\to\bar{b}$	$(P_{c_s\to b})^2$
	$b\bar{b}j\gamma$	$j\to\gamma$	5×10^{-4}
	$c\bar{c}j\gamma$	$c\to b$, $\bar{c}\to\bar{b}$, $j\to\gamma$	$(P_{c\to b})^2\cdot(5\times10^{-4})$
	$b\bar{b}jj$	$j\to\gamma$, $j\to\gamma$	$(5\times10^{-4})^2$
	$Z(\to b\bar{b})\gamma\gamma$	N/A	N/A
$t\bar{t}$	Leptonic decay	$e\to\gamma$, $e\to\gamma$	$(0.02)^2/0.02\cdot0.05/(0.05)^2$
	Semileptonic decay	$e\to\gamma$, $j\to\gamma$	$(0.02)\cdot5\times10^{-4}/(0.05)\cdot5\times10^{-4}$
$t\bar{t}\gamma$	Leptonic decay	$e\to\gamma$	0.02/0.05
	Semileptonic	$e\to\gamma$	0.02/0.05

TABLE IV. Sequence of event selection criteria at the HL-LHC applied in this analysis.

Sequence	Event selection criteria at the HL-LHC
1	Diphoton trigger condition, ≥2 isolated photons with $P_T > 25$ GeV, $\lvert\eta\rvert < 2.5$
2	≥2 isolated photons with $P_T > 30$ GeV, $\lvert\eta\rvert < 1.37$ or $1.52 < \lvert\eta\rvert < 2.37$, $\Delta R_{j\gamma} > 0.4$
3	≥2 jets identified as b jets with leading (subleading) $P_T > 40(30)$ GeV, $\lvert\eta\rvert < 2.4$
4	Events are required to contain ≤5 jets with $P_T > 30$ GeV within $\lvert\eta\rvert < 2.5$
5	No isolated leptons with $P_T > 25$ GeV, $\lvert\eta\rvert < 2.5$
6	$0.4 < \Delta R_{b\bar{b}} < 2.0$, $0.4 < \Delta R_{\gamma\gamma} < 2.0$
7	$122 < M_{\gamma\gamma}/\text{GeV} < 128$ and $100 < M_{b\bar{b}}/\text{GeV} < 150$
8	$P_T^{\gamma\gamma} > 80$ GeV, $P_T^{b\bar{b}} > 80$ GeV

3. $t\bar{t}$ and $t\bar{t}\gamma$ backgrounds

The $t\bar{t}$ background is generated at NLO in QCD using POWHEG BOX and interfaced to PYTHIA8 for parton showering and hadronization. And for the PDF set, CT10 [36] is taken. Since it mimics the signal with an electron in the final state faking a photon, we have required that the final state should include at least one lepton.[7] And the BG yield is normalized using the cross section calculated with the Top++2.0 program at NNLO in QCD which also includes soft-gluon resummation to NNLL [22]. Here we are taking $m_t = 172.5$ GeV.

A background with a similar size comes from the $t\bar{t}$ production with one photon in the final state. The $t\bar{t}\gamma$ sample is generated at LO in QCD with MADGRAPH5_AMC@NLO and interfaced with PYTHIA8 for showering and hadronization. For $t\bar{t}\gamma$, we are taking the CTEQ6L1 PDF set, and the BG yield is normalized using the cross section calculated in NLO in QCD [23]. Also, as in $t\bar{t}$, we require the final state to contain at least one lepton. In Table III, we are summarizing the main fake processes and rates also for the $t\bar{t}$ and $t\bar{t}\gamma$ backgrounds.

D. Event selections

A sequence of event selections is applied to the signal and background samples. It is clearly listed in Table IV. We follow closely the steps reported in an ATLAS conference report [30]. The goal is to obtain a pair of isolated photons and a pair of isolated b quarks. Both pairs are reconstructed near the Higgs-boson mass. In particular, the cuts $\Delta R_{\gamma\gamma} < 2.0$ and $\Delta R_{bb} < 2.0$ are imposed so as to suppress the main backgrounds which are more populated in the regions of $\Delta R_{\gamma\gamma,bb} > 2.0$; see Fig. 3.[8] We show the angular separation between photons and that between b jets for all the

[7]Here a lepton means e, μ, or τ.

[8]For larger values of $|\lambda_{3H}|$, the cuts of $\Delta R_{\gamma\gamma,bb} < 2.0$ remove more signal events compared to the SM case; see the upper left frame in Fig. 13 in Appendix A. This leads to the smaller efficiencies as shown in Table V when $\lambda_{3H} = -4$, 6, and 10. We find that the different choices of $\Delta R_{\gamma\gamma,bb}$ cuts hardly improve the signal significance and employ the same cuts taken by the ATLAS group [30].

backgrounds and the signal with $\lambda_{3H} = 1$ in the left and right frame in Fig. 3, respectively. It is clear that the majority of the signal and a very few backgrounds lie in the region $\Delta R_{\gamma\gamma} < 2$ and $\Delta R_{bb} < 2$. In Fig. 4, we show the transverse momentum distributions $P_T^{\gamma\gamma}$ and $P_T^{b\bar{b}}$ for the signal with $\lambda_{3H} = 1$ and all the backgrounds. We observe the signal tends to have a larger transverse momentum. Distributions of $\Delta R_{\gamma\gamma}$ and $P_T^{\gamma\gamma}$ with other values of λ_{3H} can be found in Appendix A, where we also show the $\Delta R_{\gamma j}$ and $M_{\gamma\gamma bb}$ distributions. The details of cuts are summarized in Table IV.

All events passing the above selection criteria are classified into two categories, depending on the pseudorapidities of the photons. If both photons appear in the barrel region ($|\eta| < 1.37$), the event is labeled as "barrel-barrel"; otherwise, it is labeled as "other."

E. Cut flows and efficiencies

We follow closely the steps used in the ATLAS conference note [30]. We compare the cut flow of our current analysis with ATLAS results for the $\lambda_{3H} = 1$ case, and they agree with each other within about 5%–15%. We show in Table V the efficiencies and event yields for Higgs-pair production in the channel $HH \to b\bar{b}\gamma\gamma$ at the HL-LHC with an integrated luminosity of 3000 fb^{-1} for various values of $\lambda_{3H} = -4, 0, 1, 2, 6, 10$. In the last row, "other/barrel ratio" is the ratio of events for the two photon candidates falling in the "other" region to those in the barrel-barrel region, after applying all the event selection cuts. The overall other/barrel ratios are all similar.

The overall signal efficiency has its peak value of 3.79% at $\lambda_{3H} = 2$, and it decreases when λ_{3H} deviates from 2. We observe that the overall efficiency drops quickly when λ_{3H}

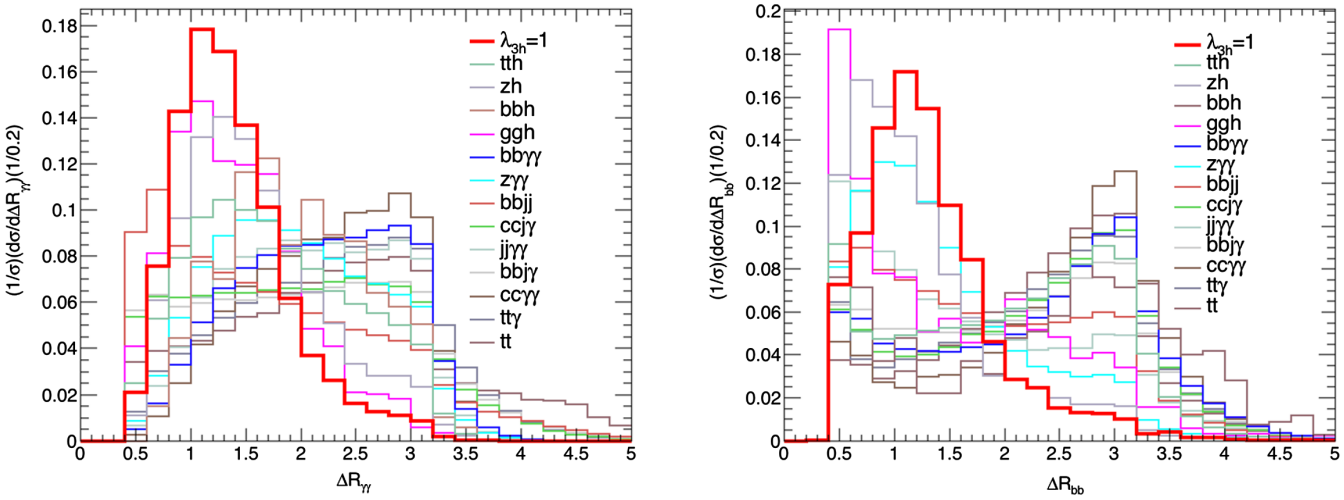

FIG. 3. The $\Delta R_{\gamma\gamma}$ and $\Delta R_{b\bar{b}}$ distributions for the signal with $\lambda_{3H} = 1$ and all the other backgrounds.

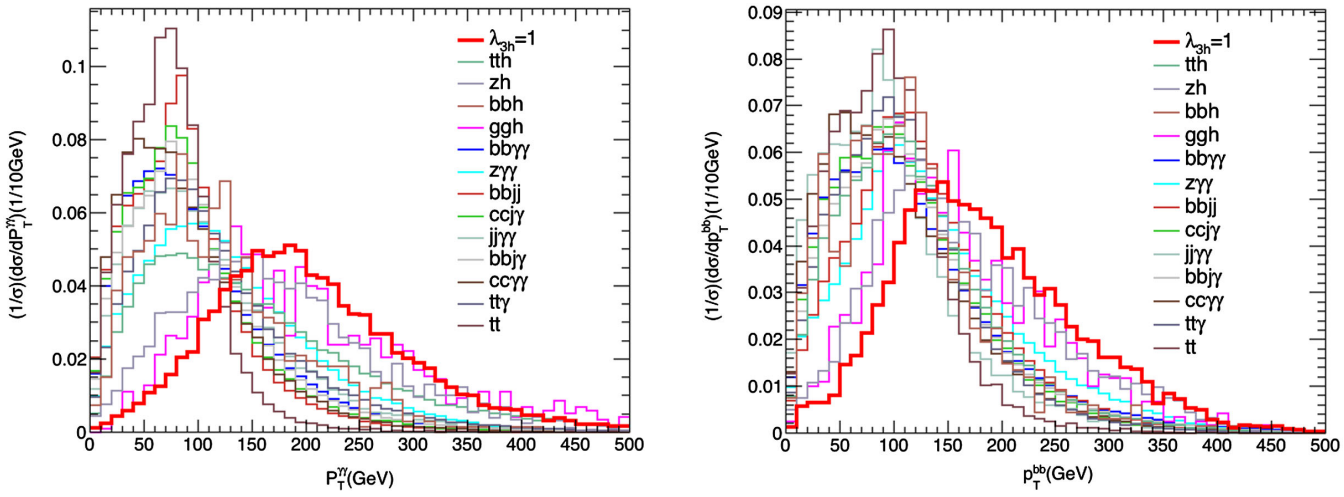

FIG. 4. The transverse momentum distributions $P_T^{\gamma\gamma}$ and $P_T^{b\bar{b}}$ for the signal with $\lambda_{3H} = 1$ and all the other backgrounds.

TABLE V. Efficiencies (%) and event yields (#): the signal cut flows for Higgs-pair production at LHC 14 TeV with an integrated luminosity of 3000 fb^{-1} for $\lambda_{3H} = -4,0,1,2,6,10$.

λ_{3H}	−4		0		1		2		6		10	
Cross section (fb)	1.45		0.25		0.12		0.06		0.48		1.97	
Cuts	Eff.%	No.#	Eff.%	No.#	Eff.%	No.#	Eff.%	No.#	Eff.%	No.#	Eff.%	No.#
1. Diphoton trigger	23.15	1007	25.63	192	27.47	99	28.94	52	20.50	295	21.01	1242
2. ≥2 isolated photons	20.79	904	23.33	175	25.21	91	26.73	48	17.82	257	18.38	1086
3-1. Jet candidates	14.58	634	17.10	128	19.07	69	20.85	38	11.62	167	12.14	717
3-2 ≥2 two b-jet	4.61	200	5.65	42	6.46	23	7.26	13	3.34	48	3.55	210
4. No. of jets ≤ 5	4.47	194	5.43	41	6.23	22	6.97	13	3.26	47	3.45	204
5. Lepton veto	4.41	192	5.36	40	6.15	22	6.88	12	3.22	46	3.41	202
6. $\Delta R_{\gamma\gamma,bb}$ cut	2.72	118	4.00	30	4.98	18	5.87	11	1.19	17	1.49	88
7-1. Higgs mass window $M_{\gamma\gamma}$	2.65	115	3.88	29	4.82	17	5.64	10	1.15	17	1.46	86
7-2. Higgs mass window M_{bb}	1.80	78	2.62	20	3.20	12	3.82	7	0.78	11	0.99	59
8. $p_{T_{\gamma\gamma}}$, $p_{T_{bb}}$ cuts	1.77	77	2.60	20	3.17	11	3.79	7	0.77	11	0.97	57
Other/barrel ratio	35.27%		36.08%		33.89%		32.66%		39.47%		37.01%	

moves to a larger value and becomes smaller than 1% when $\lambda_{3H} \gtrsim 4$, while when λ_{3H} becomes smaller and starts to take on negative values, it decreases to 3.17% at the SM value of $\lambda_{3H} = 1$ and reaches 1.77% at $\lambda_{3H} = -4$. This is because of the strong destructive (constructive) interference between the triangle and box diagrams for the positive (negative) values of λ_{3H} and the enhancement of kinematical features of the triangle diagram for $|\lambda_{3H}| > 1$. Thus, these two effects are combined to give a strong dependence of the $\Delta R_{\gamma\gamma,bb}$ distributions on λ_{3H}, therefore leading to the strong dependence of the signal efficiency on λ_{3H}. On the other hand, the number of signal events, which is given by the product of the cross section, signal efficiency, and luminosity of 3000 fb^{-1}, is only 7 at $\lambda_{3H} = 2$, but it becomes 11 at the SM value of $\lambda_{3H} = 1$. Note that one may have the same number of signal events also at $\lambda_{3H} = 6$.

The cut flow tables of all the backgrounds in terms of efficiencies at the HL-LHC are presented in Appendix B.

F. Analysis and results

Here we show the main results of our analysis in Table VI—the resultant signal rates for various λ_{3H} against all the backgrounds. The last column is for the number of generated events in each sample. The statistical uncertainties originating from the limited number of generated events are estimated by dividing each of the background and signal samples into roughly $O(10)$ subsamples. The fluctuations among the subsamples are then taken as the uncertainty of the sample. We have made detailed comparisons with the results from ATLAS [30]. In general, we agree, except for ggH and $t\bar{t}$. In the ggH sample, we figure out that about half of the disagreement is caused by the differences in the b-tagging algorithm and detector simulations, while, for the $t\bar{t}$ sample, our estimation is made based on the DELPHES3 algorithm for electron reconstruction and identification, which is about 20 times more efficient than that taken by ATLAS.

More precisely, in the ggH sample, our number of the ggH background is 6.60, which is 2.4 times larger than the ATLAS number of 2.74 [30]. By noting that the ggH sample is dominated by b quarks from showering processes, we find a part of the difference can be attributed to a different b-tagging algorithm taken in our work: Ours is from Ref. [32] while, in the ATLAS paper, the algorithm from Ref. [37] is used. If we use the same algorithm taken in the ATLAS paper, we find the number of background reduces to about 5, which is still a bit above the ATLAS number 2.74. We also find another reason in the detector simulations, but, again, it is not enough to fully explain the difference. Indeed, a similar observation has been recently made by the authors of Ref. [13]. When they used the same selection cuts as ATLAS, the result was also larger than the ATLAS result but consistent with ours.

We note that the kinematic distributions for the signal with different λ_{3H} would not be very different, as seen by the ratio (O/B) in the last of Table VI, which are more or less the same for different λ_{3H}. On the other hand, the ratio (O/B) for the backgrounds, on average, is larger than the signal, which means the backgrounds are, in general, more forward. We further note that the combined significance obtained by splitting events into two categories of barrel-barrel and other is improved by 3% over the total one when $\lambda_{3H} = 1$. For our analysis, we use the combined significance.

The most dominant one in the single-Higgs associated backgrounds is $t\bar{t}H$ followed by ggH. The single-Higgs associated processes contribute about 23 events to the total background. Meanwhile, the dominant ones in nonresonant backgrounds are $b\bar{b}\gamma\gamma$ and $b\bar{b}j\gamma$, with each contributing 19 events to the total background. A similar size of background comes from combined $c\bar{c}\gamma\gamma \oplus c\bar{c}j\gamma \oplus jj\gamma\gamma$,

TABLE VI. HL-LHC yields: Expected number of signal and background events at the HL-LHC assuming 3000 fb^{-1}. We separate the backgrounds into three categories (see the text). The significance for $\lambda_{3H} = 1$ (SM) is also shown; see Eq. (9). The combined significance is given by the square root of the sum of the squares of the barrel-barrel and other significances.

Samples	Total	Barrel-barrel	Other (end cap)	Ratio (O/B)	# of gen. events
$H(b\bar{b})H(\gamma\gamma)$, $\lambda_{3H} = -4$	77.14 ± 0.94	57.03 ± 0.75	20.11 ± 0.34	0.35 ± 0.01	3×10^5
$H(b\bar{b})H(\gamma\gamma)$, $\lambda_{3H} = 0$	19.50 ± 0.20	14.33 ± 0.16	5.17 ± 0.13	0.36 ± 0.01	3×10^5
$H(b\bar{b})H(\gamma\gamma)$, $\lambda_{3H} = 1$	11.42 ± 0.082	8.53 ± 0.092	2.89 ± 0.048	0.34 ± 0.01	3×10^5
$H(b\bar{b})H(\gamma\gamma)$, $\lambda_{3H} = 2$	6.82 ± 0.05	5.14 ± 0.04	1.68 ± 0.03	0.33 ± 0.01	3×10^5
$H(b\bar{b})H(\gamma\gamma)$, $\lambda_{3H} = 6$	11.03 ± 0.21	7.91 ± 0.23	3.12 ± 0.10	0.39 ± 0.02	3×10^5
$H(b\bar{b})H(\gamma\gamma)$, $\lambda_{3H} = 10$	57.46 ± 1.01	41.94 ± 0.60	15.52 ± 0.62	0.37 ± 0.02	3×10^5
$ggH(\gamma\gamma)$	6.60 ± 0.69	4.50 ± 0.71	2.10 ± 0.30	0.47 ± 0.10	6×10^6
$t\bar{t}H(\gamma\gamma)$	13.21 ± 0.23	9.82 ± 0.19	3.39 ± 0.17	0.35 ± 0.02	10^6
$ZH(\gamma\gamma)$	3.62 ± 0.16	2.44 ± 0.16	1.18 ± 0.08	0.48 ± 0.05	10^6
$b\bar{b}H(\gamma\gamma)$	0.15 ± 0.024	0.11 ± 0.027	0.04 ± 0.014	0.40 ± 0.16	10^6
$b\bar{b}\gamma\gamma$	18.86 ± 0.9	11.15 ± 0.7	7.71 ± 0.5	0.69 ± 0.06	1.1×10^7
$c\bar{c}\gamma\gamma$	7.53 ± 1.06	4.79 ± 1.10	2.74 ± 0.81	0.57 ± 0.21	10^7
$jj\gamma\gamma$	3.34 ± 0.46	1.59 ± 0.31	1.75 ± 0.32	1.10 ± 0.29	10^7
$b\bar{b}j\gamma$	18.77 ± 1.00	10.40 ± 0.83	8.37 ± 0.63	0.80 ± 0.09	10^7
$c\bar{c}j\gamma$	5.52 ± 1.4	3.94 ± 1.0	1.58 ± 0.6	0.40 ± 0.18	10^7
$b\bar{b}jj$	5.54 ± 0.5	3.81 ± 0.3	1.73 ± 0.2	0.45 ± 0.06	5×10^6
$Z(b\bar{b})\gamma\gamma$	0.90 ± 0.03	0.54 ± 0.02	0.36 ± 0.02	0.67 ± 0.04	10^7
$t\bar{t}$ ($\geq$1 leptons)	4.98 ± 0.23	3.04 ± 0.12	1.94 ± 0.21	0.64 ± 0.07	10^7
$t\bar{t}\gamma$ ($\geq$1 leptons)	3.61 ± 0.21	2.29 ± 0.15	1.32 ± 0.15	0.58 ± 0.08	10^7
Total background	92.63 ± 2.5	58.42 ± 2.0	34.21 ± 1.4	0.59 ± 0.03	
Significance Z	1.163	1.090	0.487		
Combined significance			1.194		

in which either hard or showering c quarks are faking b jets basically. Among the nonresonant backgrounds, $b\bar{b}jj$ contributes the least. Including $t\bar{t}$ and $t\bar{t}\gamma$ in which one or two electrons are faking photons, we note that more than one-half of the total background is due to fakes.

In Fig. 5, we show the resultant invariant-mass distributions of the two photon (upper) and two b (lower) candidates for the signal on top of all the backgrounds. We have applied all the selection cuts except for the cut on $M_{\gamma\gamma}$ ($M_{b\bar{b}}$) in the upper (lower) frame. The photon peak

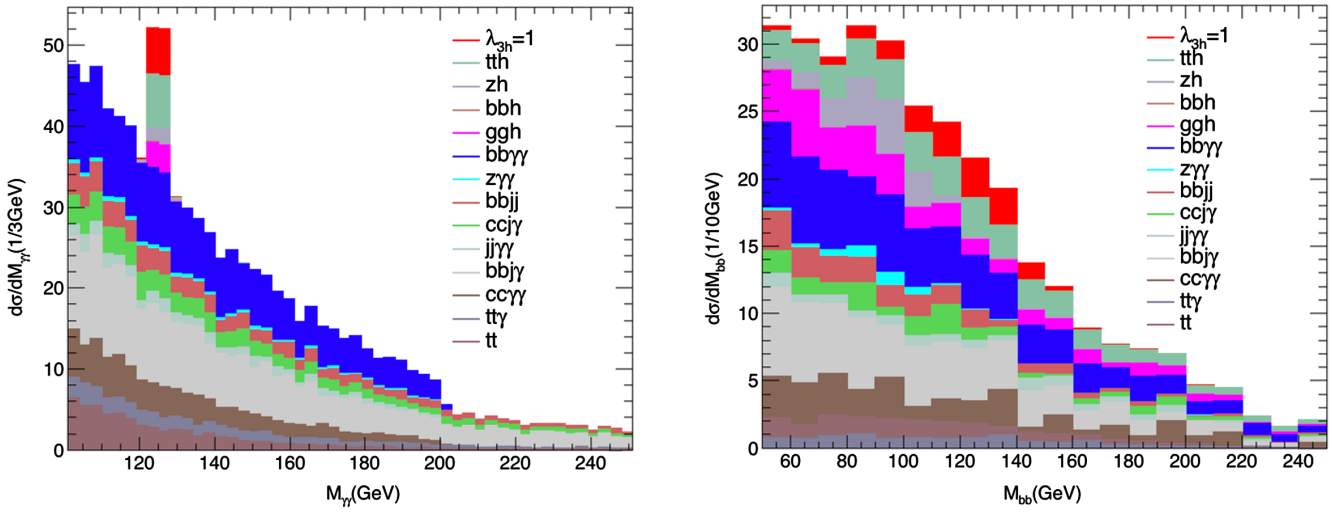

FIG. 5. The $M_{\gamma\gamma}$ (left) and $M_{b\bar{b}}$ (right) distributions for the signal on top of all the backgrounds at the HL-LHC.

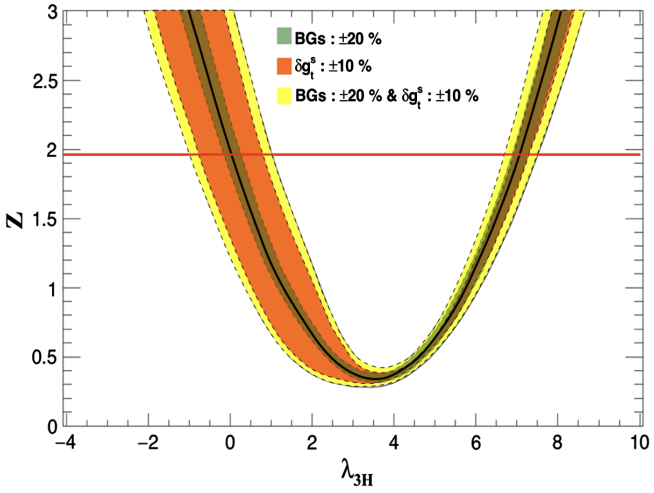

FIG. 6. HL-LHC: Significance of the signal over the background versus λ_{3H}. The orange and green bands represents the impact of the uncertainties associated with the top-Yukawa coupling and the estimation of backgrounds, respectively, and the yellow one the impact of both of the uncertainties. The black solid line is for the case when $g_t^S = 1$ and $b = 92.63$; see Table VI.

$M_{\gamma\gamma} \sim 125$ GeV is very clear, while that of $M_{b\bar{b}} \sim 125$ GeV is rather broad, due to the b-jet resolution.

In Fig. 6, we show the significance defined by

$$Z = \sqrt{2 \cdot [((s+b) \cdot \ln(1+s/b) - s)]}, \tag{9}$$

where s and b represent the numbers of signal and background events, respectively. The central curve is for the case when the top-Yukawa coupling takes on the SM value of $g_t^S = 1$ and $b = 92.63$; see Table VI. The orange and green bands have been obtained by varying the top-Yukawa coupling by 10%[9] ($|\delta g_t^S| \leq 0.1$) and the total background yield by 20% ($|\delta b/b| \leq 0.2$), respectively. The yellow band has been obtained by considering both of the uncertainties simultaneously. The uncertainty associated with the estimation of backgrounds may arise from pileup, the photon and b-tagging efficiencies, several fake rates, the choices of renormalization and factorizations scales and PDF, etc. We note that the δg_t^S effect becomes larger when λ_{3H} decreases from 3.5. For $\lambda_{3H} \gtrsim 3.5$, the δb effect could be comparably important. Given that all the uncertainties can be minimized and the top Yukawa at the SM value, the 95% C.L. sensitivity region for λ_{3H} is $0 < \lambda_{3H} < 7.1$. However, given the worst uncertainties with $\delta g_t^S = \pm 0.1$ and $\delta b/b = \pm 0.2$, the sensitivity range widens to $-1.0 < \lambda_{3H} < 7.6$. We note that the lower boundary of the 95% C.L. region of λ_{3H} is sensitive to the top-Yukawa g_t^S, while the impact of the uncertainty associated with the estimation of backgrounds turns out minor upon the 20% variation over the total background.

[9]In our work, we also take account of the effect of the 10% uncertainty of the top-Yukawa coupling on the ggH and $t\bar{t}H$ backgrounds while neglecting its effect on the Higgs decay mode into two photons, since it is dominated by the W loops. Incidentally, we have taken the SM values for the Higgs couplings to b quarks and W bosons for $H \to \gamma\gamma$.

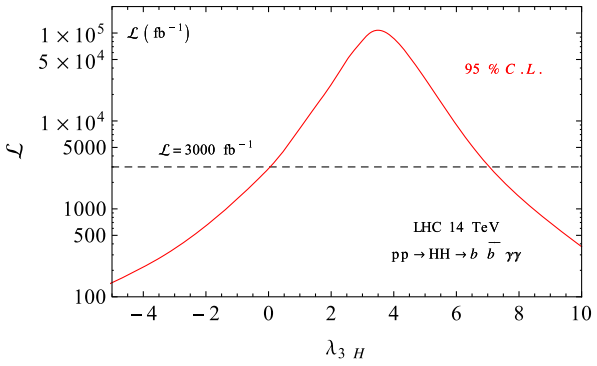

FIG. 7. HL-LHC: Required luminosity for 95% C.L. sensitivity at the 14 TeV HL-LHC versus λ_{3H}. Here we assume that the top-Yukawa coupling takes the SM value.

Finally, we show in Fig. 7 the luminosity required to achieve 95% C.L. sensitivity versus λ_{3H}. We observe that the SM value of $\lambda_{3H} = 1$ can be established only with about 8.5 ab^{-1} luminosity. Note that the required luminosity peaks at $\lambda_{3H} \simeq 3.5$, while the $gg \to HH$ production takes its smallest value at $\lambda_{3H} \simeq 2.5$; see Fig. 1. This is because of the strong dependence of the signal efficiency on λ_{3H} induced by the substantial interference between the triangle and box diagrams together with, especially for $|\lambda_{3H}| > 1$, the enhancement of kinematical features of the triangle diagram or the smaller Higgs-pair invariant mass of $M_{\gamma\gamma bb}$, the wider angular separations of $\Delta R_{\gamma\gamma,bb}$, and the smaller transverse momenta of $P_T^{\gamma\gamma,bb}$.

IV. SIMULATIONS, EVENT SELECTIONS, AND ANALYSIS AT THE HL-100 TEV COLLIDER

In this section, through the $HH \to b\bar{b}\gamma\gamma$ channel, we estimate how well one can measure the λ_{3H} coupling at a 100 TeV hadron collider assuming a nominal luminosity of 3 ab^{-1} or at the HL-100 TeV hadron collider. We basically follow the procedures that we took in the last section for the 14 TeV HL-LHC case, though some selection cuts may be changed because of the much higher center-of-mass energy. We have taken a crude estimate projected from the current LHC detectors for the P_T and η coverage for jets, leptons, and photons without any specific detector designs available for the 100 TeV hadron collider.

A. Parton-level event generations and detector simulations

The same signal and backgrounds are considered as in the 14 TeV case. The Monte Carlo generators, the cross

TABLE VII. The same as in Table I but for a 100 TeV hadron collider. In the row for $b\bar{b}H(\to\gamma\gamma)$, 5FS stands for the five-flavor scheme. Note that, except the $ggH(\to\gamma\gamma)$ background which is generated at NLO, all the signal and backgrounds are generated at LO and normalized to the cross sections computed at the accuracy denoted in order in QCD.

Signal				
Signal process	Generator/parton shower	$\sigma \cdot$ BR [fb]	Order in QCD	PDF used
$gg \to HH \to b\bar{b}\gamma\gamma$ [20]	MG5_aMC@NLO/PYTHIA8	4.62	NNLO + NNLL	NNPDF2.3LO

Backgrounds					
Background (BG)	Process	Generator/parton shower	$\sigma \cdot$ BR [fb]	Order in QCD	PDF used
Single-Higgs associated BG	$ggH(\to\gamma\gamma)$ [20]	POWHEG BOX/PYTHIA8	1.82×10^3	NNNLO	CT10
	$t\bar{t}H(\to\gamma\gamma)$ [20]	PYTHIA8/PYTHIA8	7.29×10^1	NLO	
	$ZH(\to\gamma\gamma)$ [20]	PYTHIA8/PYTHIA8	2.54×10^1	NNLO	
	$b\bar{b}H(\to\gamma\gamma)$ [38]	PYTHIA8/PYTHIA8	1.96×10^1	NNLO (5FS)	
Nonresonant BG	$b\bar{b}\gamma\gamma$	MG5_aMC@NLO/PYTHIA8	4.93×10^3	LO	CTEQ6L1
	$c\bar{c}\gamma\gamma$	MG5_aMC@NLO/PYTHIA8	4.54×10^4	LO	
	$jj\gamma\gamma$	MG5_aMC@NLO/PYTHIA8	5.38×10^5	LO	
	$b\bar{b}j\gamma$	MG5_aMC@NLO/PYTHIA8	1.44×10^7	LO	
	$c\bar{c}j\gamma$	MG5_aMC@NLO/PYTHIA8	4.20×10^7	LO	
	$b\bar{b}jj$	MG5_aMC@NLO/PYTHIA8	1.60×10^{10}	LO	
	$Z(\to b\bar{b})\gamma\gamma$	MG5_aMC@NLO/PYTHIA8	9.53×10^1	LO	
$t\bar{t}$ and $t\bar{t}\gamma$ BG [20] ($\geq$1 lepton)	$t\bar{t}$	MG5_aMC@NLO/PYTHIA8	1.76×10^7	NLO	CT10
	$t\bar{t}\gamma$	MG5_aMC@NLO/PYTHIA8	4.18×10^4	NLO	CTEQ6L1

sections, and the orders of QCD calculation are shown in Table VII. Note that, for some backgrounds, the orders in QCD are different compared to the 14 TeV case. Otherwise, the calculational methods taken for the signal and background samples are essentially the same as those what we employed for the HL-LHC.

On the other hand, preselection cuts, detector energy resolutions, tagging efficiencies, and fake rates may undergo significant changes because of different designs and projected performance of the detectors in the future. Below, we describe in detail what we use in our analysis.

(i) Preselection cuts, which are imposed in order to avoid any divergence in the parton-level calculations, are modified as follows to match the wider η coverage of future particle detectors:

$$\begin{aligned} &P_{T_j} > 20\ \text{GeV}, \quad && P_{T_b} > 20\ \text{GeV}, \\ &P_{T_\gamma} > 25\ \text{GeV}, \quad && P_{T_l} > 10\ \text{GeV}, \\ &|\eta_j| < 6, \quad && |\eta_\gamma| < 6, \\ &|\eta_l| < 6, \quad && \Delta R_{jj,ll,\gamma\gamma,\gamma j,jl,\gamma l} > 0.4, \\ &M_{jj} > 25\ \text{GeV}, \quad && M_{bb} > 45\ \text{GeV}, \\ &60 < M_{\gamma\gamma} < 200\ \text{GeV}. \end{aligned}$$

(ii) Fast detector simulation and analysis at the HL-100 TeV hadron collider are performed using DELPHES3 [31] with the FCChh template. For the energy resolution of the detector, we have chosen the "medium" detector performance for electromagnetic calorimeter (ECAL) and hadronic calorimeter (HCAL) [20],[10] because we could get the best significance for this choice. In the medium performance scenario, the ECAL energy resolution is given by

$$\Delta E/E|_{\text{ECAL}} = \sqrt{0.01^2 + 0.1^2\ \text{GeV}/E}$$

and the HCAL energy resolution by

$$\Delta E/E|_{\text{HCAL}} = \begin{cases} \sqrt{0.03^2 + 0.5^2\ \text{GeV}/E} & \text{for } |\eta| \leq 4, \\ \sqrt{0.05^2 + 1.0^2\ \text{GeV}/E} & \text{for } 4 < |\eta| \leq 6. \end{cases}$$

Furthermore, we set the magnetic field at 6 T, and the jet energy scale of 1.135 is taken to get the correct peak position at M_H in the invariant mass distribution of the b-quark pair in the signal process.

(iii) For the b-jet tagging efficiency and related jet fake rates, we are taking $\epsilon_b = 75\%$, $P_{c\to b} = 10\%$, and $P_{j\to b} = 1\%$ [20].

(iv) For the photon efficiency and jet fake rate, we are taking $\epsilon_\gamma = 95\%$ ($|\eta_\gamma| \leq 1.5$), 90% ($1.5 < |\eta_\gamma| \leq 4$), 80% ($4 < |\eta_\gamma| \leq 6$), and $P_{j\to\gamma} = 1.35 \times 10^{-3}$ [20].

[10]In Ref. [20], three scenarios of ECAL and HCAL performance are considered: "low," "medium," and "high."

TABLE VIII. Production cross section times the branching ratio $\sigma \cdot \mathrm{BR}(HH \to b\bar{b}\gamma\gamma)$ at the 100 TeV pp collider.

λ_{3H}	−4	0	1	2	6	10
$\sigma\cdot\mathrm{BR}(HH\to b\bar{b}\gamma\gamma)$ [fb]	46.97	8.99	4.62	2.32	13.61	57.78

For the $e \to \gamma$ fake rate, with a separation between the barrel and end cap regions at $|\eta| = 2$, we take $P_{e\to\gamma} = 2\%(5\%)$ in the barrel (end cap) region as a reference [30].

B. Signal event samples

The signal event samples are generated in exactly the same way as in the HL-LHC case. We show the production cross section times the branching ratio at the 100 TeV pp collider for six selected values of $\lambda_{3H} = -4, 0, 1, 2, 6, 10$ in Table VIII.

C. Background samples

As in the HL-LHC case, we categorize the backgrounds into single-Higgs associated backgrounds, nonresonant backgrounds, and $t\bar{t}$ and $t\bar{t}\gamma$ backgrounds. The information is summarized in Table VII. Note that the $t\bar{t}$ sample is generated with MADGRAPH5_AMC@NLO, and for showering, hadronization, and decays of unstable particles only PYTHIA8 is used.[11] Otherwise, the descriptions of the backgrounds are the same as in the HL-LHC case.

The cross sections increase as we move from 14 to 100 TeV. The signal cross section increases by a factor of about 40. The cross section for the single-Higgs associated backgrounds increases by a factor of about 15 except $t\bar{t}H(\to\gamma\gamma)$: The increment factor for the $t\bar{t}H(\to\gamma\gamma)$ process is about 50. The cross section for the $Z(\to b\bar{b})\gamma\gamma$ process increases by a factor of about 20, while the increment factor of the other nonresonant backgrounds is about 40. The cross sections for the $t\bar{t}$-related backgrounds increase by about 30 times. As we will show, the nonresonant backgrounds constitute more than 75% of the total backgrounds. Roughly, the cross sections for the signal and dominant background processes increase by a factor of about 40. Finally, in Table IX, we summarize the faking rates of nonresonant and $t\bar{t}$-related backgrounds which we use for the HL-100 TeV collider.

D. Event selections

A sequence of event selections is applied to the signal and background samples; see Table X. We basically follow our HL-LHC analysis but using a more relaxed ΔR condition to inclusively cover the broad range of λ_{3H} still allowed after the HL-LHC era. Also considered are the wider $|\eta|$ coverage at 100 TeV and the more energetic jets and photons.

The distributions in $\Delta R_{\gamma\gamma}$, ΔR_{bb}, $P_T^{\gamma\gamma}$, P_T^{bb}, $\Delta R_{\gamma b}$, and $M_{\gamma\gamma bb}$ are very similar to the case of HL-LHC. We collect some of them in Appendix A in order not to interrupt smooth reading of the main text.

E. Cut flows and efficiencies

We closely follow the procedures that we employed for the HL-LHC. We show in Table XI the efficiencies and event yields for Higgs-pair production in the channel $HH \to b\bar{b}\gamma\gamma$ with $\lambda_{3H} = -4, 0, 1, 2, 6, 10$ and an integrated luminosity of 3000 fb^{-1} at the 100 TeV collider.

The overall signal efficiency has its peak value of 8.01% at $\lambda_{3H} = 2$, and its behavior is similar to that at 14 TeV with ∼2% when $\lambda_{3H} \gtrsim 4$, 6.79% at the SM value of $\lambda_{3H} = 1$, and 3.98% at $\lambda_{3H} = -4$. On the other hand, the number of signal event is 557 at $\lambda_{3H} = 2$, and it becomes 941 at the SM value of $\lambda_{3H} = 1$. Note that one may have a similar number of signal events at $\lambda_{3H} = 6$.

The cut flow table of all the backgrounds in terms of efficiencies at the HL-100 TeV hadron collider is presented in Appendix B.

F. Analysis and results

Here we show the main results of the analysis for the 100 TeV hadron collider; see Table XII. Among the single-Higgs associated backgrounds, the major ones come from ggH and $t\bar{t}H$, comprising about 20% of the total background. Meanwhile, the dominant ones in nonresonant backgrounds are $b\bar{b}jj$ followed by $b\bar{b}j\gamma$ which make up about 60% of the total background. Including other backgrounds, we note that 70% of the total background is due to fakes. Being contrary to the HL-LHC case, the combined significance achieved is much higher: $Z = 9.981$ at the SM value of $\lambda_{3H} = 1$, which is mainly because of much higher signal event rates though the signal to background ratios are similar at HL-LHC and HL-100 TeV collider.

In Fig. 8, we show the resultant invariant-mass distributions of the two photon (upper) and two b (lower) candidates for the signal on top of all the backgrounds at the HL-100 TeV collider, as similar to HL-LHC in Fig. 5. We observe similar behavior as in the HL-LHC case.

Since the achieved significance is high enough, we try to estimate how well one can measure the λ_{3H} coupling at the HL-100 TeV hadron collider. In the left frame in Fig. 9, we show the number of signal events N as a function of λ_{3H}. To obtain the curve, we assume the luminosity of 3 ab^{-1} and take into account the λ_{3H}-dependent overall signal efficiencies; see Table XI. One may find the values of N for some representative choices of λ_{3H} in Table XII. On the other hand, the solid horizontal line shows the number of signal events s, as an example, when the input value of λ_{3H} or $\lambda_{3H}^{\mathrm{in}}$ takes the SM value of 1. The dotted lines delimit

[11] Note that PYTHIA6 is used for the $ggH(\to\gamma\gamma)$ process at the HL-LHC.

TABLE IX. The main fake processes and the corresponding faking rates in each sample of nonresonant and $t\bar{t}(\gamma)$ backgrounds. We recall that $P_{j\to\gamma} = 1.35 \times 10^{-3}$, $P_{c\to b} = P_{c_s\to b} = 0.1$ [20], and $P_{e\to\gamma} = 2\%$ (5%) in the barrel (end cap) calorimeter region.

Background (BG)	Process	Fake process	Fake rate
Nonresonant BG	$b\bar{b}\gamma\gamma$	N/A	N/A
	$c\bar{c}\gamma\gamma$	$c \to b$, $\bar{c} \to \bar{b}$	$(0.1)^2$
	$jj\gamma\gamma$	$c_s \to b$, $\bar{c}_s \to \bar{b}$	$(0.1)^2$
	$b\bar{b}j\gamma$	$j \to \gamma$	1.35×10^{-3}
	$c\bar{c}j\gamma$	$c \to b$, $\bar{c} \to \bar{b}$, $j \to \gamma$	$(0.1)^2 \cdot (1.35 \times 10^{-3})$
	$b\bar{b}jj$	$j \to \gamma$, $j \to \gamma$	$(1.35 \times 10^{-3})^2$
	$Z(\to b\bar{b})\gamma\gamma$	N/A	N/A
$t\bar{t}$	Leptonic decay	$e \to \gamma$, $e \to \gamma$	$(0.02)^2/0.02 \cdot 0.05/(0.05)^2$
	Semileptonic decay	$e \to \gamma$, $j \to \gamma$	$(0.02) \cdot 1.35 \times 10^{-3}/(0.05) \cdot 1.35 \times 10^{-3}$
$t\bar{t}\gamma$	Leptonic decay	$e \to \gamma$	0.02/0.05
	Semileptonic	$e \to \gamma$	0.02/0.05

TABLE X. Sequence of event selection criteria at the HL-100 TeV hadron collider applied in this analysis.

Sequence	Event selection criteria at the HL-100 TeV hadron collider
1	Diphoton trigger condition, ≥2 isolated photons with $P_T > 30$ GeV, $\|\eta\| < 5$
2	≥2 isolated photons with $P_T > 40$ GeV, $\|\eta\| < 3$, $\Delta R_{j\gamma} > 0.4$
3	≥2 jets identified as b jets with leading (subleading) $P_T > 50(40)$ GeV, $\|\eta\| < 3$
4	Events are required to contain ≤5 jets with $P_T > 40$ GeV within $\|\eta\| < 5$
5	No isolated leptons with $P_T > 40$ GeV, $\|\eta\| < 3$
6	$0.4 < \Delta R_{b\bar{b}} < 3.0$, $0.4 < \Delta R_{\gamma\gamma} < 3.0$
7	$122.5 < M_{\gamma\gamma}/\text{GeV} < 127.5$ and $90 < M_{b\bar{b}}/\text{GeV} < 150$
8	$P_T^{\gamma\gamma} > 100$ GeV, $P_T^{b\bar{b}} > 100$ GeV

TABLE XI. The same as in Table V but at the 100 TeV hadron collider with an integrated luminosity of 3 ab^{-1}.

λ_{3H}	−4		0		1		2		6		10	
Cross section (fb)	46.97		8.99		4.62		2.32		13.61		57.78	
Cuts	Eff.%	No.#	Eff.%	No.#	Eff.%	No.#	Eff.%	No.#	Eff.%	No.#	Eff.%	No.#
1. Diphoton trigger	56.06	78988	57.78	15582	58.99	8176	60.00	4176	53.44	21818	53.82	93293
2. ≥2 isolated photons	36.31	51158	39.21	10575	41.29	5722	43.40	3021	32.39	13225	32.94	57105
3-1. Jet candidates	29.07	40965	32.77	8838	35.36	4901	37.94	2641	23.87	9746	24.74	42881
3-2 ≥2 two b jet	9.57	13492	11.41	3076	12.75	1767	14.18	987	7.31	2986	7.65	13252
4. No. of jets ≤5	9.03	12724	10.60	2860	11.79	1634	13.04	907	6.99	2856	7.29	12638
5. Lepton veto	9.03	12724	10.60	2860	11.79	1634	13.04	907	6.99	2856	7.29	12637
6. $\Delta R_{\gamma\gamma,bb}$ cut	8.32	11730	10.08	2718	11.34	1572	12.57	875	5.92	2419	6.39	11023
7-1. Higgs mass window $M_{\gamma\gamma}$	7.78	10968	9.35	2523	10.51	1456	11.57	805	5.55	2268	5.97	10341
7-2. Higgs mass window M_{bb}	6.14	8650	7.32	1974	8.23	1140	9.08	632	4.48	1830	4.77	8264
8. $p_{T_{\gamma\gamma}}$, $p_{T_{bb}}$ cuts	3.98	5604	5.61	1514	6.79	941	8.01	557	1.84	753	2.21	3838
Other/barrel ratio	31.64%		30.14%		30.05%		29.18%		33.03%		31.26%	

the $1-\sigma$ region considering the statistical error of $\Delta s = \sqrt{s+b}$ with $b = 9147.63$. For this purpose, we generate another pseudo dataset for the signal. By locating the points where the N curve and the horizontal lines meet, one can obtain the two center values of output λ_{3H} and the corresponding two regions of $1-\sigma$ error. Note that, usually, there is a twofold ambiguity in this approach. By repeating this procedure for different input values of

TABLE XII. The same as in Table VI but at the HL-100 TeV hadron collider with an integrated luminosity of 3 ab^{-1}.

Samples	Total	Barrel-barrel	Other (end cap)	Ratio (O/B)	# of gen. events
$H(b\bar{b})H(\gamma\gamma)$, $\lambda_{3H}=-4$	5604.46 ± 63.36	4257.36 ± 57.90	1347.10 ± 23.22	0.32 ± 0.007	3×10^5
$H(b\bar{b})H(\gamma\gamma)$, $\lambda_{3H}=0$	1513.56 ± 14.81	1163.04 ± 14.09	350.52 ± 3.57	0.30 ± 0.005	3×10^5
$H(b\bar{b})H(\gamma\gamma)$, $\lambda_{3H}=1$	941.37 ± 7.65	723.86 ± 6.64	217.51 ± 3.66	0.30 ± 0.006	3×10^5
$H(b\bar{b})H(\gamma\gamma)$, $\lambda_{3H}=2$	557.36 ± 1.93	431.45 ± 1.87	125.91 ± 1.21	0.29 ± 0.003	3×10^5
$H(b\bar{b})H(\gamma\gamma)$, $\lambda_{3H}=6$	753.18 ± 6.02	566.18 ± 5.59	187.00 ± 5.33	0.33 ± 0.010	3×10^5
$H(b\bar{b})H(\gamma\gamma)$, $\lambda_{3H}=10$	3838.33 ± 36.82	2924.25 ± 32.11	914.08 ± 28.01	0.31 ± 0.010	3×10^5
$ggH(\gamma\gamma)$	890.47 ± 72.91	742.97 ± 58.43	147.50 ± 20.51	0.20 ± 0.03	10^6
$t\bar{t}H(\gamma\gamma)$	868.73 ± 8.53	659.33 ± 12.94	209.40 ± 7.04	0.32 ± 0.01	9.63×10^5
$ZH(\gamma\gamma)$	168.86 ± 5.91	122.91 ± 4.68	45.95 ± 1.69	0.37 ± 0.02	10^6
$b\bar{b}H(\gamma\gamma)$	9.82 ± 0.59	7.00 ± 0.58	2.82 ± 0.25	0.40 ± 0.05	10^6
$b\bar{b}\gamma\gamma$	770.42 ± 23.48	514.96 ± 20.81	255.46 ± 15.10	0.50 ± 0.04	1.1×10^7
$c\bar{c}\gamma\gamma$	222.88 ± 40.55	111.44 ± 32.55	111.44 ± 26.92	1.00 ± 0.38	1.1×10^7
$jj\gamma\gamma$	32.28 ± 3.23	20.98 ± 3.99	11.30 ± 2.34	0.54 ± 0.15	10^7
$b\bar{b}j\gamma$	1829.13 ± 75.08	1288.34 ± 45.27	540.79 ± 49.79	0.42 ± 0.04	1.1×10^7
$c\bar{c}j\gamma$	293.81 ± 40.11	216.49 ± 36.71	77.32 ± 32.97	0.36 ± 0.16	1.1×10^7
$b\bar{b}jj$	3569.73 ± 209.93	2294.83 ± 207.69	1274.90 ± 189.68	0.56 ± 0.10	3.43×10^6
$Z(b\bar{b})\gamma\gamma$	54.87 ± 3.79	35.72 ± 3.36	19.15 ± 2.02	0.54 ± 0.08	10^6
$t\bar{t}$ ($\geq$1 leptons)	59.32 ± 7.40	38.32 ± 5.79	21.00 ± 5.61	0.55 ± 0.17	1.1×10^7
$t\bar{t}\gamma$ ($\geq$1 leptons)	105.68 ± 8.22	62.53 ± 5.07	43.15 ± 7.95	0.69 ± 0.14	10^6
Total background	8876.00 ± 243.07	6115.82 ± 227.41	2760.18 ± 202.67	0.45 ± 0.04	
Significance Z	9.823	9.082	4.087		
Combined significance		9.959			

λ_{3H}, we can obtain the center output λ_{3H} values together with the regions of $1-\sigma$ error, as shown in the right frame in Fig. 9.

The black-shaded region (delimited by the black dashed lines) in the right frame in Fig. 9 shows the 1-σ errors versus the input values of $\lambda_{3H}^{\rm in}$ with the luminosity of 3 ab^{-1}. Incidentally, the black solid line shows the center values of output λ_{3H} values or $\lambda_{3H}^{\rm out}$ along the $\lambda_{3H}^{\rm out}=\lambda_{3H}^{\rm in}$ line denoted by the thin dotted line. We note that there exists a bulk region of $2.6 \lesssim \lambda_{3H} \lesssim 4.8$ in which one cannot pin down the λ_{3H} coupling. We find that the bulk region reduces to $3.1 \lesssim \lambda_{3H} \lesssim 4.3$ assuming the luminosity of 30 ab^{-1} as shown by the red-shaded region (delimited by the red dashed lines) in the same frame in Fig. 9.

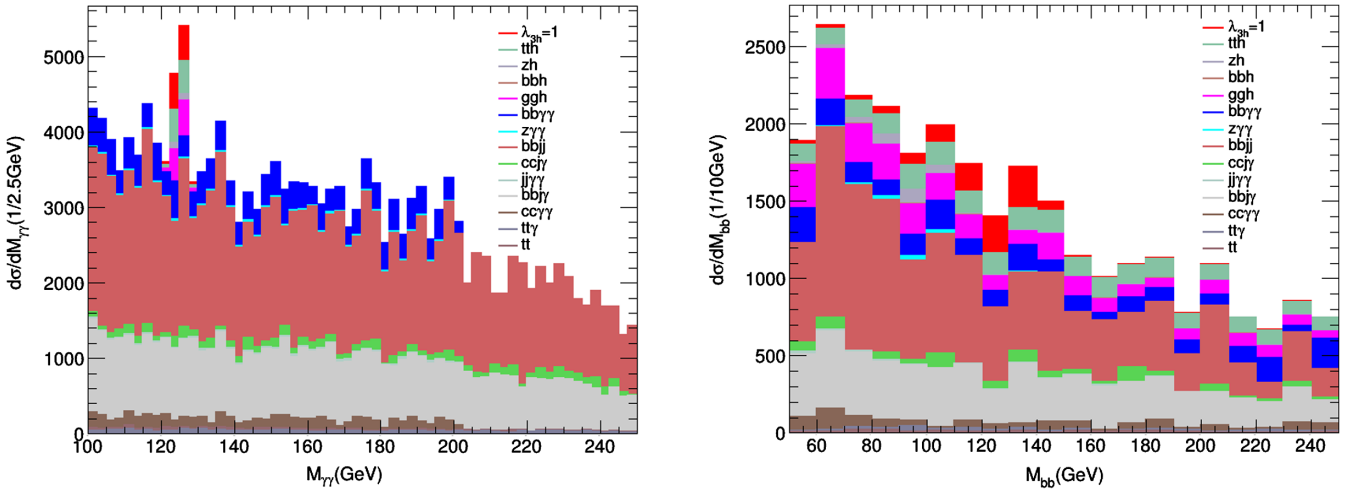

FIG. 8. The $M_{\gamma\gamma}$ (left) and $M_{b\bar{b}}$ (right) distributions for the signal on top of all the backgrounds at the HL-100 TeV hadron collider.

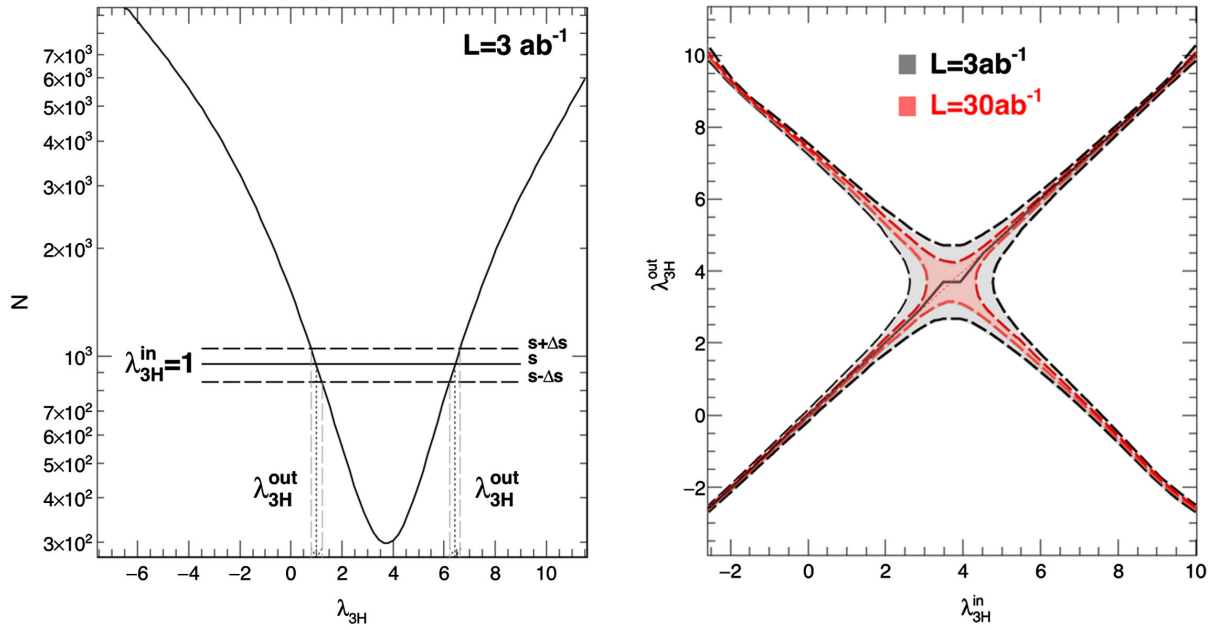

FIG. 9. HL-100 TeV: (Left) The number of signal events N versus λ_{3H} with 3 ab^{-1}. The horizontal solid line is for the number of signal events s when $\lambda_{3H}^{\mathrm{in}} = 1$, and the dashed lines for $s \pm \Delta s$ with the statistical error of $\Delta s = \sqrt{s+b}$. (Right) The $1-\sigma$ error regions versus the input values of $\lambda_{3H}^{\mathrm{in}}$ assuming 3 ab^{-1} (black) and 30 ab^{-1} (red).

Even though it would be difficult to pin down the λ_{3H} coupling in the bulk region, one goes a bit away from it and is able to measure the coupling with a high precision as indicated by the narrowness of the 1-σ error regions. And, the twofold ambiguity can be lifted up by exploiting the kinematical differences found in the distributions of $\Delta R_{\gamma\gamma}$, $P_T^{\gamma\gamma}$, and $M_{\gamma\gamma bb}$ when λ_{3H} takes on different values; see Fig. 15. Keeping these all in mind, in Fig. 10, we show the regions in which one can determine the λ_{3H} coupling within an absolute error of 0.3 (either upper or lower error) along the $\lambda_{3H}^{\mathrm{out}} = \lambda_{3H}^{\mathrm{in}}$ line assuming 3 (upper panel) and 30 ab^{-1} (lower panel). The green-shaded regions around $\lambda_{3H} = 3.5$ denote the bulk regions. We observe that, when $\lambda_{3H} \lesssim 1.6(2.4)$ or $\lambda_{3H} \gtrsim 5.9(5.3)$, one can pin down the λ_{3H} coupling with an absolute error smaller than 0.3 assuming 3 (30) ab^{-1}. At the SM value of $\lambda_{3H} = 1$, specifically, we observe that the coupling can be measured with about 20% (7%) accuracy assuming the integrated luminosity of 3 (30) ab^{-1}. Our results are about 2 times better than those reported in Ref. [39] and comparable with those in Ref. [40] taking account of the more sophisticated and comprehensive treatment of the background processes taken in this work.

Before moving to the next section, we comment that the bulk region can be shifted by adopting a different set of selection cuts, and it may help if it turns out that λ_{3H} falls into the bulk region in the future.

V. FURTHER IMPROVEMENTS ENVISAGED

In our analysis, we are taking the SM cross sections of $\sigma(gg \to HH) = 45.05$ fb and $\sigma(gg \to HH) = 1749$ fb at

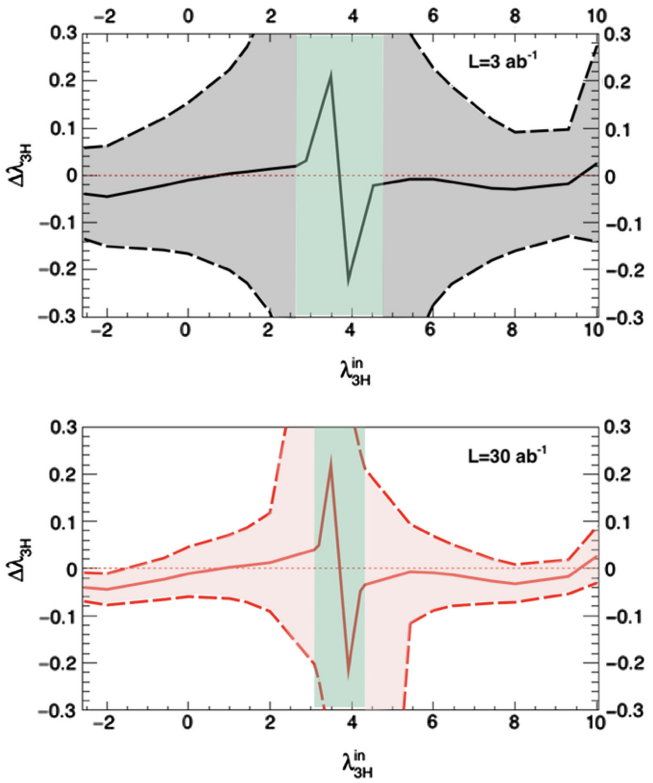

FIG. 10. HL-100 TeV: $\Delta\lambda_{3H} = \lambda_{3H}^{\mathrm{out}} - \lambda_{3H}^{\mathrm{in}}$ versus $\lambda_{3H}^{\mathrm{in}}$ along the $\lambda_{3H}^{\mathrm{out}} = \lambda_{3H}^{\mathrm{in}}$ line with 3 (upper) and 30 ab^{-1} (lower). The lines are the same as in the right frame in Fig. 9. We consider $|\Delta\lambda_{3H}| \leq 0.3$ to find the regions in which one can pin down the λ_{3H} coupling with an absolute error smaller than 0.3.

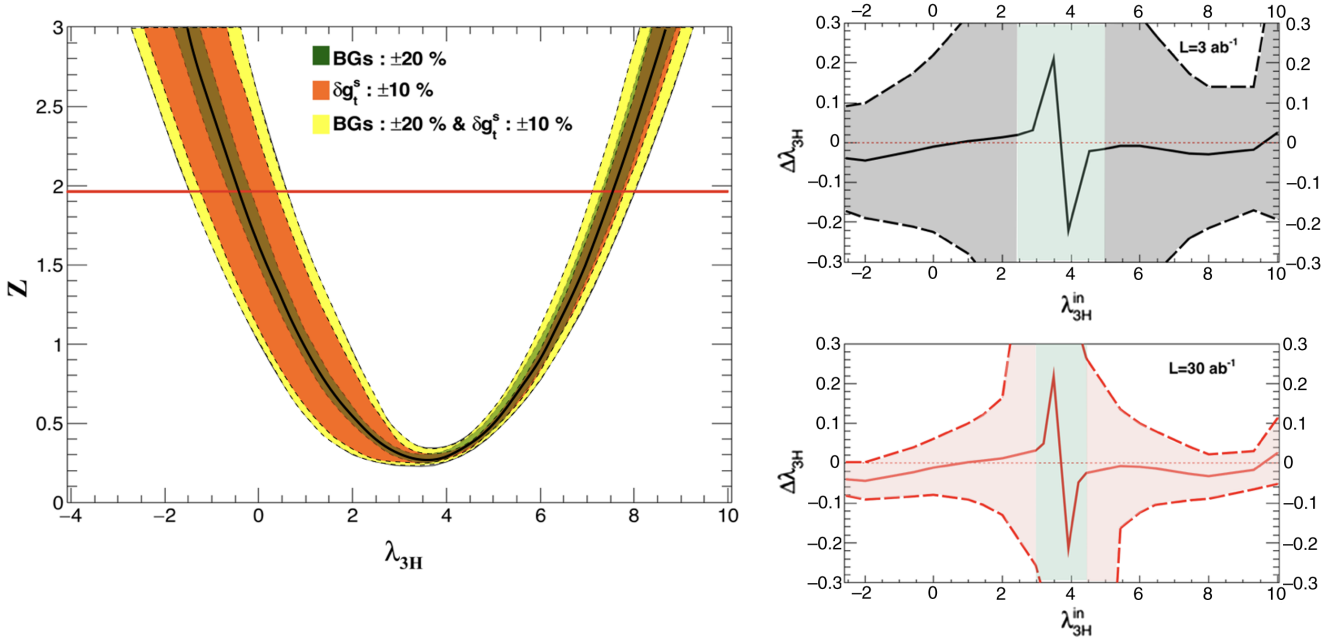

FIG. 11. (Left) HL-LHC: The same as in Fig. 6 but taking the NNLO cross section $\sigma(gg \to HH) = 36.69$ fb in the FT approximation. (Right) HL-100 TeV: The same as in Fig. 10 but taking the NNLO cross section $\sigma(gg \to HH) = 1224$ fb in the FT approximation.

14 and 100 TeV, respectively, which are calculated at NNLO accuracy including NNLL gluon resummation in the infinite top-quark mass approximation. We have taken these values of cross sections to confirm, especially, the ATLAS results [30]. Recently, the NLO corrections considering full top-quark mass dependence have been available [41,42]. The calculation reveals that the full top-quark mass dependence is vital to get reliable predictions for Higgs-boson-pair production. Precisely, the total cross section is reduced by 14% at 14 TeV compared to that obtained by the Born improved Higgs effective field theory (HEFT) in which the infinite top mass approximation is taken. At 100 TeV, the larger reduction of 24% is found.

At the moment, as suggested in Ref. [43], the best way to incorporate the finite top-quark mass effects at NNLO might be by adopting the FT approximation [16,44] in which the full top-quark mass dependence is considered only in the real radiation while the HEFT is taken in the virtual part. At NNLO in the FT approximation, $\sigma(gg \to HH) = 36.69$ fb and $\sigma(gg \to HH) = 1224$ fb at 14 and 100 TeV, respectively [43]. We observe 20% (30%) reduction at 14 (100) TeV compared to the cross sections used in Secs. III and IV. To see the impact of the reduced cross sections on our main results, in Fig. 11, we show the signal significance over the background versus λ_{3H} at the HL-LHC (left) and the regions in which one can determine the λ_{3H} coupling with an absolute error of 0.3 at the HL-100 TeV collider (right). At 14 TeV with 3000 fb^{-1}, the trilinear coupling is constrained to be $-1.5 < \lambda_{3H} < 8.1$ at 95% C.L., taking account of the uncertainties associated with the top-Yukawa coupling and the estimation of backgrounds. Taking the central line, the 95% C.L. sensitivity region for λ_{3H} is $-0.4 < \lambda_{3H} < 7.5$, which becomes broader by the amount of ± 0.4 compared to the results presented in Sec. III.[12] At 100 TeV, we find a little bit broader bulk regions of $2.4 \lesssim \lambda_{3H} \lesssim 5.0$ and $3.0 \lesssim \lambda_{3H} \lesssim 4.4$ with 3 and 30 ab^{-1}, respectively, compared to the results presented in Sec. IV.[13] And, λ_{3H} can be measured with an accuracy of 30% (10%) with an integrated luminosity of 3 (30) ab^{-1} when it takes on its SM value of 1. We observe that the effects of the reduced cross sections are less significant in the case with 30 ab^{-1} at 100 TeV in which the number of signal events is comparable to or larger than that of backgrounds.

The QCD corrections also affect the ratio $\sigma(gg \to HH)/\sigma(gg \to HH)_{\rm SM}$ which is used to obtain the cross sections for non-SM values of λ_{3H}. The QCD corrections depend on λ_{3H} and become larger when λ_{3H} deviates from the SM value 1 due to the nontrivial interference between the triangle and box diagrams [42]. We observe that the ratio increases by about 10% (35%) at $\lambda_{3H} = -1(5)$; see Fig. 12. It is clear that the QCD corrections are less significant than the uncertainties associated with the top-Yukawa coupling; see Fig. 2. In this respect, we have not taken account of the λ_{3H}-dependent QCD corrections on the

[12]Recall that the corresponding region is $0 < \lambda_{3H} < 7.1$ if the NNLO + NNLL cross section of 45.05 fb is taken.

[13]Recall that, when the NNLO + NNLL cross section of 1749 fb is taken at 100 TeV, the bulk regions are $2.6(3.1) < \lambda_{3H} < 4.8(4.3)$ and λ_{3H} can be measured with an accuracy of 20% (7%) at its SM value with 3 (30) ab^{-1}.

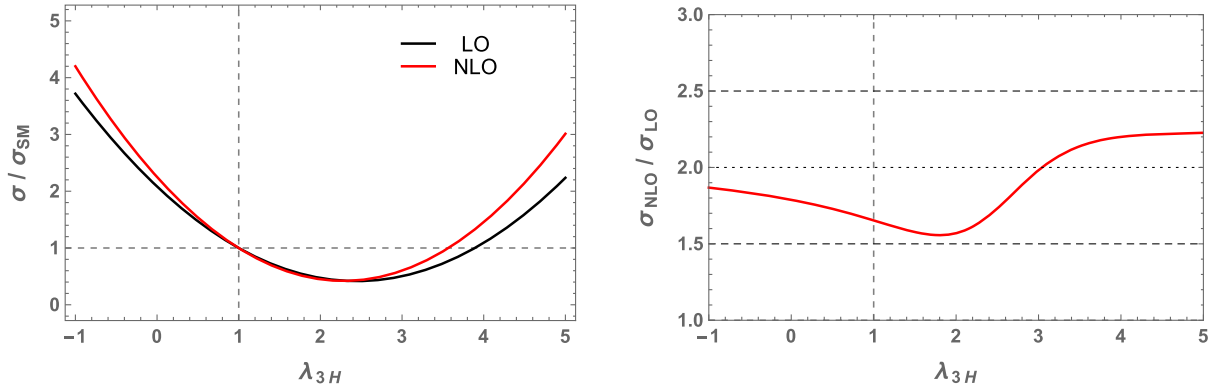

FIG. 12. (Left) The ratio $\sigma(gg \to HH)/\sigma(gg \to HH)_{\rm SM}$ versus λ_{3H} at LO (black) and NLO (red) at 14 TeV. We have taken the NLO cross sections considering full top-quark mass dependence. (Right) The ratio $\sigma^{\rm NLO}(gg \to HH)/\sigma^{\rm LO}(gg \to HH)$ versus λ_{3H} at 14 TeV. We refer to Ref. [42] for absolute cross sections as functions of λ_{3H}.

ratio $\sigma(gg \to HH)/\sigma(gg \to HH)_{\rm SM}$ in this work.[14] On the other hand, when $|\lambda_{3H}|$ is significantly larger than 1, vertex corrections proportional to λ_{3H}^3 appear at the amplitude level. This may bring a sizable distortion to $\sigma(gg \to HH)/\sigma(gg \to HH)_{\rm SM}$. In this case, it might be practical to consider λ_{3H} as an effective parameter, not as a fundamental one.

Note that the $P_T^{\gamma\gamma,bb}$ and $M_{\gamma\gamma bb}$ distributions are affected by the QCD corrections at NLO and NNLO as shown in, for example, Refs. [42,43]. For more precise predictions at the HL-LHC and HL-100 TeV collider and to lift up the twofold ambiguity in λ_{3H} especially, one may need to incorporate them in the future.

The PDF set of CTEQ6L1 taken to calculate the nonresonant backgrounds does not include the use of data from LHC experiments. To study the impact of the LHC data on PDF, instead of CTEQ6L1, we take the PDF set of CT14LO [45] and resimulate all the nonresonant backgrounds at 14 TeV. Taking the example of $b\bar{b}\gamma\gamma$ background, which is one of the two most severe nonresonant backgrounds, we obtain the overall efficiency of 4.34×10^{-3} by generating 10^7 events. This is very similar to the efficiency of 4.49×10^{-3} obtained using CTEQ6L1; see Table XIII. Actually, we observe that the two efficiencies in each step of cut flow coincide within less than 10% and there are no significant differences in kinematic distributions caused by CT14LO. Meanwhile, the real effect of CT14LO is the reduction of the cross sections for the nonresonant backgrounds. For $b\bar{b}\gamma\gamma$, as an example, it reduces to 112 fb.[15] Compared to the cross section of 140 fb obtained using CTEQ6L1, the cross section reduces by 20%.

Furthermore, the preselection cuts listed in Eq. (6) may not be enough to avoid the double counting problems in the nonresonant background samples. To address this point, we implement Mangano (MLM) matching [46,47]. We observe that there are no significant differences in kinematic distributions due to MLM matching. For details of the matching precesses and the calculation of the merged cross sections, we refer to Appendix C. Taking account of the NNLO cross section $\sigma(gg \to HH) = 36.69$ fb in the FT approximation and the λ_{3H}-dependent QCD corrections, we obtain the central 95% C.L. sensitivity region of $-0.4 < \lambda_{3H} < 6.9$ at 14 TeV; see the black dash-dotted line in Fig. 21. Incorporating the impact of CT14LO and the reduction of the nonresonant background cross sections by MLM matching, the region reduces to $0.1 < \lambda_{3H} < 6.6$; see the blue dashed line in Fig. 21.

Last but not least, we also take into account the contribution from the Higgs production accompanied by a hard $b\bar{b}$ pair via gluon fusion at 14 TeV. For this purpose, we calculate the $gg \to Hb\bar{b}$ process, which is supposed to be the leading hard process for the contribution [13]. Adopting the cuts suggested in Ref [13] and using MG5_aMC@NLO and NNPDF2.3LO, we obtain $\sigma(gg \to Hb\bar{b}) \simeq 4.8$ fb at 14 TeV.[16] Then we find a selection efficiency of 2.7% for the process $gg \to H(\to \gamma\gamma)b\bar{b}$, which leads to the 0.9 event at 14 TeV with 3 ab^{-1} after all the selection cuts are applied. Therefore, the total number of the $ggH(\to \gamma\gamma)$ background may increase into $6.6 + 0.9 = 7.5$ after including the hard process. We conclude that about 10% of the background might come from the hard $b\bar{b}$ pair production at 14 TeV.

VI. CONCLUSIONS

One of the major goals of the HL-LHC and HL-100 TeV hadron collider is to unfold the mystery of the EWSB

[14]Taking account of the λ_{3H}-dependent QCD corrections, at 14 TeV, we observe that the central 95% C.L. sensitivity region reduces from $-0.4 < \lambda_{3H} < 7.5$ to $-0.4 < \lambda_{3H} < 6.9$, since the QCD corrections enhance the signal cross section for $\lambda_{3H} \lesssim 1$ and $\lambda_{3H} \gtrsim 2.5$.

[15]For other backgrounds at 14 TeV, see σ presented in Table XV.

[16]This is about 4 times smaller than the corresponding cross section of ~22 fb at 27 TeV [13].

mechanism, which is related to the origin of mass. We have investigated the trilinear self-coupling of the Higgs boson in Higgs-pair production using the most promising channel $pp \to HH \to \gamma\gamma b\bar{b}$ with a fully comprehensive signal-background analysis. It turns out that various fake backgrounds, including $c \to b$, $j \to \gamma$, and $e \to \gamma$, are among the most dominant backgrounds that have to be discriminated against the signal.

The high-luminosity option of the LHC (HL-LHC) with an integrated luminosity of 3000 fb^{-1} can constrain the trilinear coupling only by $-1.0 < \lambda_{3H} < 7.6$ at 95% C.L. after taking into account the uncertainties associated with the top-Yukawa coupling and estimation of total background. This is unfortunate if the trilinear coupling takes on the SM value; it cannot be confirmed at the HL-LHC due to very small event rates. On the other hand, a much larger signal event rate at the HL-100 hadron collider enables one to pin down the value of λ_{3H} with an absolute error smaller than 0.3, except for a near-bulk region $1.6 < \lambda_{3H} < 5.9$ $(2.4 < \lambda_{3H} < 5.3)$, with an integrated luminosity of 3 (30) ab^{-1}. If λ_{3H} takes on the SM value, it can be measured with an accuracy of 20% (7%) with a luminosity of 3 (30) ab^{-1}.

Before closing, we offer a few more comments.

(1) Variations of cross sections with λ_{3H} for different production channels differ from one another. Indeed, if λ_{3H} falls at the minimum of $\sigma(gg \to HH)$, one can use, for example, $q\bar{q}^{(\prime)} \to W/Z + HH$ to probe the trilinear coupling. See Fig. 1.

(2) We do not investigate the vector-boson fusion mechanism in this work. Though its cross section is at least one order magnitude smaller than gluon fusion, it has an additional handle to discriminate against backgrounds due to two very energetic and forward jets in the final state.

(3) Currently, the reconstruction of the b-quark momentum is far from ideal as can be shown from the invariant mass $M_{b\bar{b}}$ spectrum. We expect that the b-jet tagging and b-jet reconstruction can be substantially improved with deep learning techniques in the future, such that the invariant mass cut on $M_{b\bar{b}}$ can be much more effective.

(4) In many other Higgs-sector extensions of the SM, there usually exist heavy neutral scalar bosons, which can be produced via gluon fusion and decays into Higgs-boson pair. Our approach of signal-background analysis can be adopted to analyze such kinds of models. Although specialized cuts tailored for particular models may generate higher significance, our approach can be applied in general.

(5) Adopting the most recent NNLO calculations in the FT approximation, the inclusive cross section is reduced by 20% at 14 TeV compared to the NNLO + NNLL cross section, and, accordingly, the 95% sensitivity range of λ_{3H} broadens by about 10%. On the other hand, the inclusive cross section is reduced by 30% at 100 TeV which results in about 20% increment of bulk regions. And the accuracy at $\lambda_{3H} = 1$ worsens to 30% (10%) with 3 (30) ab^{-1}.

(6) When we compare our HL-100 TeV results to those of Ref. [20], we found that their results have higher significance. This is because we have considered more backgrounds in our analysis such as the category of single-Higgs backgrounds and $bbjj$.

(7) We observe that the nonresonant backgrounds could be significantly reduced by reflecting the impact of the LHC data on PDF and considering MLM matching.

ACKNOWLEDGMENTS

We thank Tie-Jiun Hou for helpful comments on PDFs. We also thank Olivier Mattelaer and Stefan Prestel for helpful comments on MLM matching and DJR distribution in MADGRAPH5_AMC@NLO with PYTHIA8. This work was supported by the National Research Foundation of Korea (NRF) Grant No. NRF-2016R1E1A1A01943297. K. C. was supported by the MoST of Taiwan under Grant No. MOST-105-2112-M-007-028-MY3. J. P. was supported by NRF Grant No. NRF-2018R1D1A1B07051126.

APPENDIX A: KINEMATICAL DISTRIBUTIONS FOR THE SIGNAL AND BACKGROUNDS AT THE HL-LHC AND HL-100 TEV HADRON COLLIDER

In Fig. 13, we show the $\Delta R_{\gamma\gamma}$, $P_T^{\gamma\gamma}$, $\Delta R_{\gamma b}$, and $M_{\gamma\gamma bb}$ distributions for the signal taking $\lambda_{3H} = -4$, 0, 1, 2, 6, and 10 at the HL-LHC. We observe that the $M_{\gamma\gamma bb}$ distribution becomes narrower and softer for the larger values of $|\lambda_{3H}|$ due to the s-channel Higgs propagator.

In the left frame in Fig. 14, we show the angular separation between one of the photons and one of the b quarks at the HL-LHC for the SM signal ($\lambda_{3H} = 1$) and all the backgrounds considered in this work. The signal tends to have relatively larger $\Delta R_{\gamma b}$, implying that γ and b originated from the signal are more or less back to back. The right frame in Fig. 14 is for the invariant mass distributions $M_{\gamma\gamma bb}$.

Figure 15 is for some distributions at the HL-100 TeV hadron collider. Most of the distributions are very similar to those at the HL-LHC.

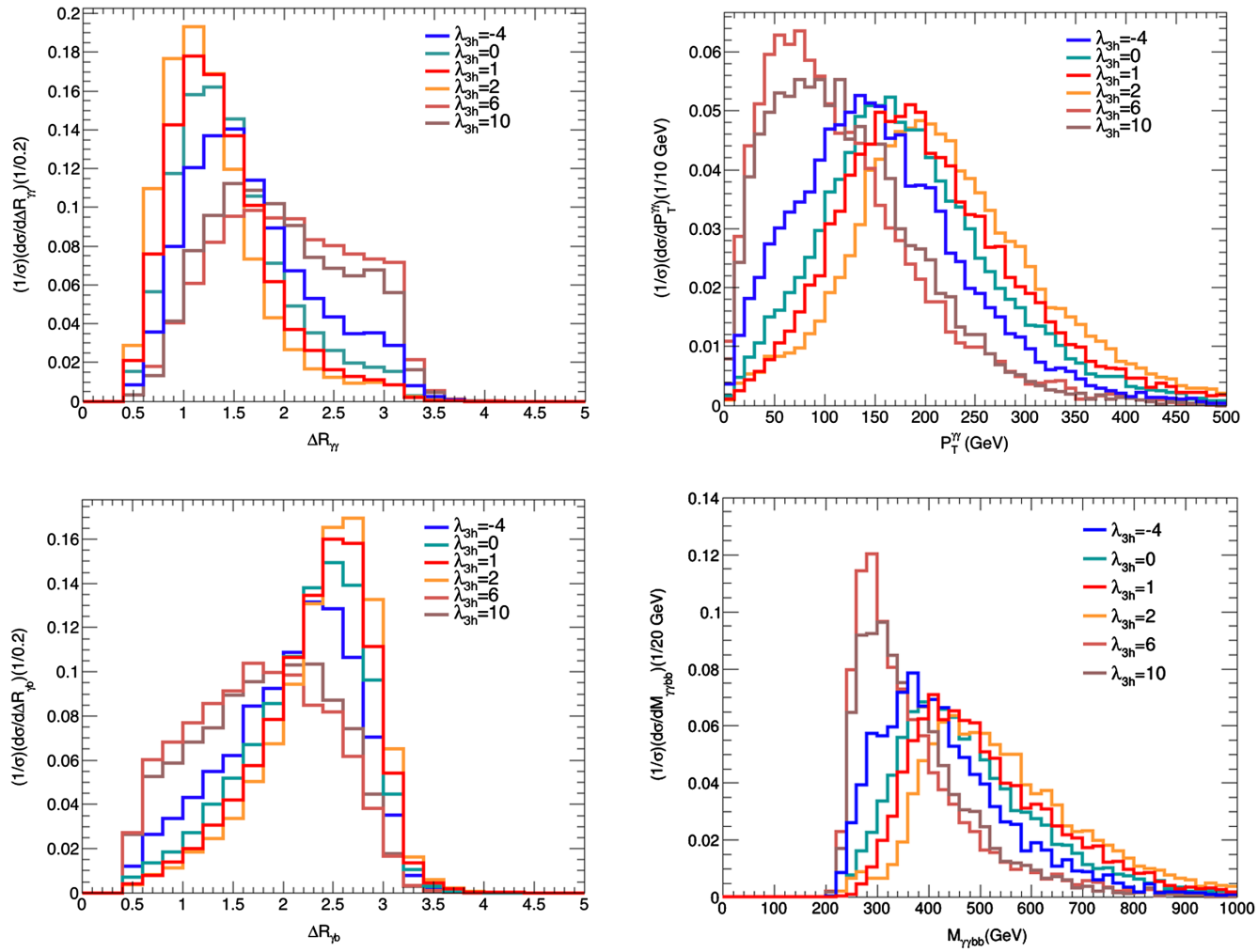

FIG. 13. HL-LHC: The $\Delta R_{\gamma\gamma}$, $P_T^{\gamma\gamma}$, $\Delta R_{\gamma b}$, and $M_{\gamma\gamma bb}$ distributions for the signal taking $\lambda_{3H} = -4$, 0, 1, 2, 6, and 10.

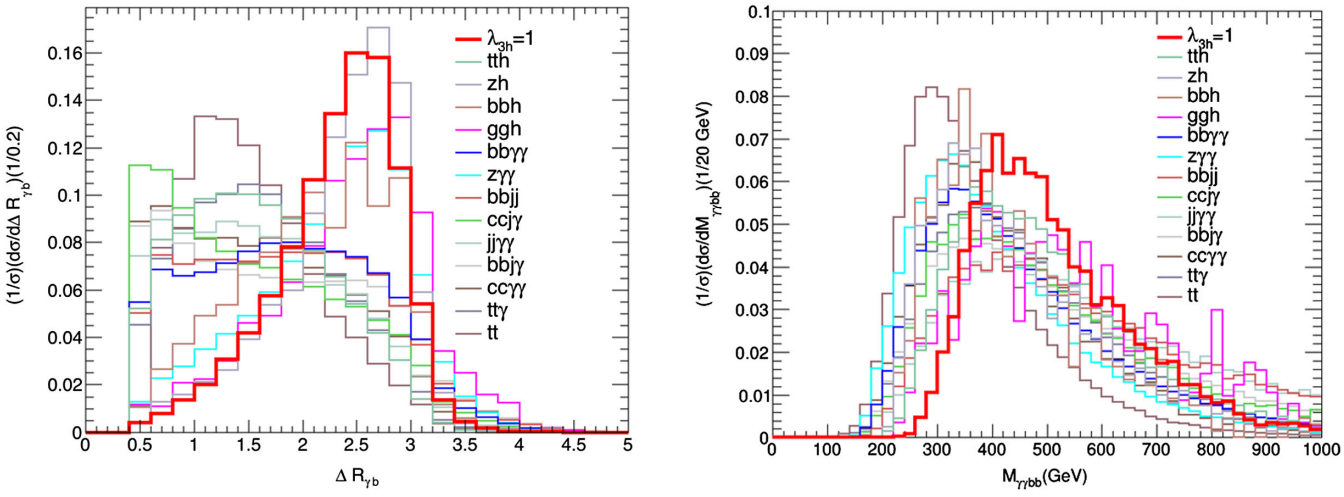

FIG. 14. HL-LHC: The $\Delta R_{\gamma b}$ and $M_{\gamma\gamma bb}$ distributions for the SM signal ($\lambda_{3H} = 1$) and all the backgrounds considered in this work.

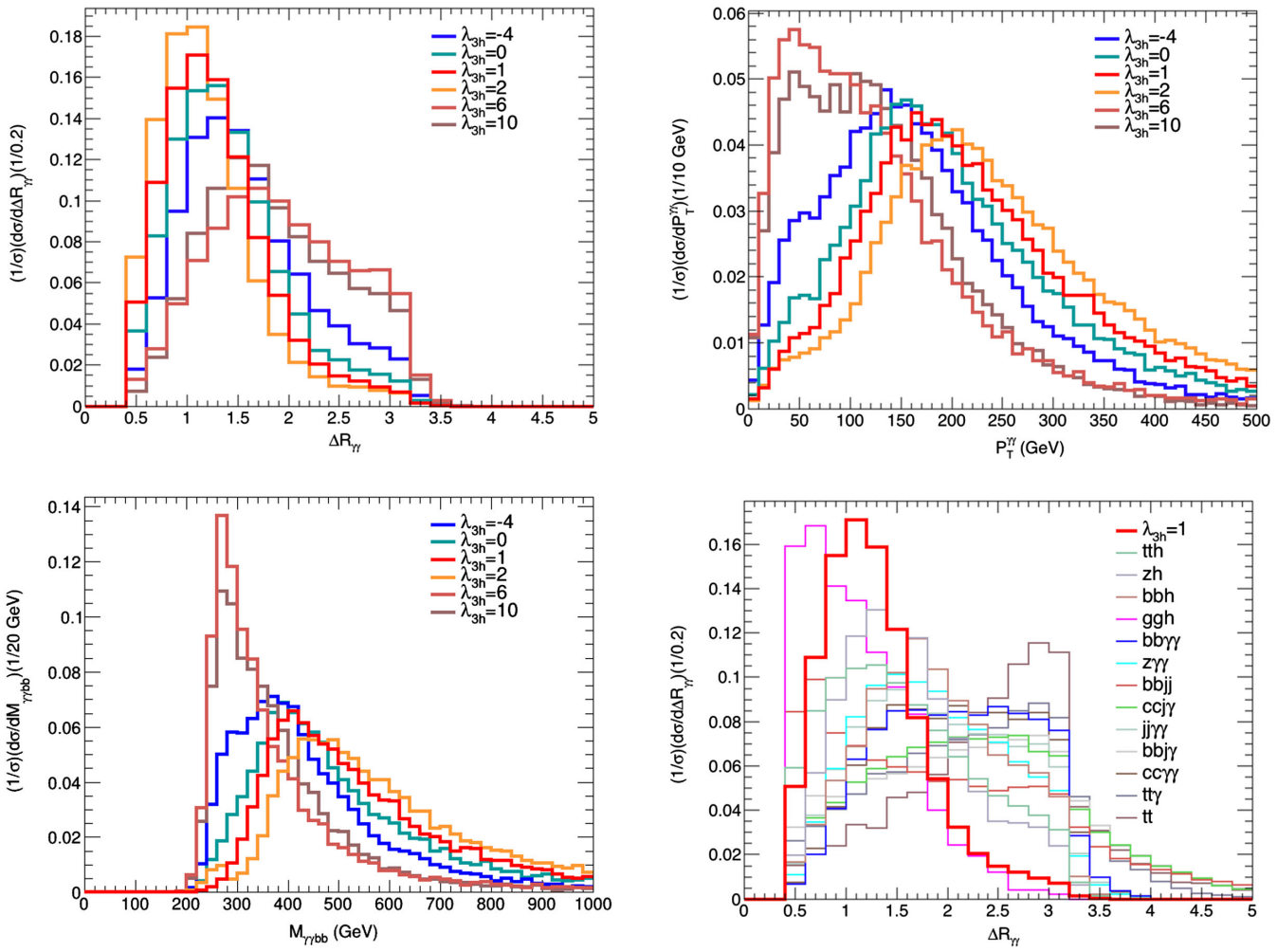

FIG. 15. HL-100 TeV: The $\Delta R_{\gamma\gamma}$ (upper left), $P_T^{\gamma\gamma}$ (upper right), and $M_{\gamma\gamma bb}$ (lower left) distributions for the signal taking $\lambda_{3H} = -4$, 0, 1, 2, 6, and 10. In the lower right frame, the $\Delta R_{\gamma\gamma}$ distributions for the SM signal ($\lambda_{3H} = 1$) and all the backgrounds are compared.

APPENDIX B: CUT FLOW TABLES FOR ALL THE BACKGROUNDS AT THE HL-LHC AND HL-100 TEV HADRON COLLIDER

In this Appendix, we present the cut flow tables for all the backgrounds at the HL-LHC and HL-100 TeV hadron collider; see Tables XIII and XIV. We note that the lepton-veto cut does not affect the $t\bar{t}$ related BGs in which electrons are faking photons.

APPENDIX C: ON THE CROSS SECTIONS OF NONRESONANT BACKGROUNDS

For the nonresonant continuum backgrounds of $b\bar{b}\gamma\gamma$, $c\bar{c}\gamma\gamma$, $jj\gamma\gamma$, $b\bar{b}j\gamma$, $c\bar{c}j\gamma$, $b\bar{b}jj$, and $Z(b\bar{b})\gamma\gamma$, we have estimated the cross sections by applying the generator-level preselection cuts listed in Eq. (6). As explained in the main text, in each background, we consider a process with an additional hard parton[17] at the matrix-element level to capture the bulk of the NLO corrections.

In our estimation, there might be a worry of double counting between the leading process and the subleading one with an additional hard parton when generated background event samples are interfaced with PYTHIA8 for showering and hadronization. To study the double counting issue, taking the PDF set of CT14LO, we consider the following three types of cross sections:

(i) $\sigma_{\text{Eq. (6)}}$ *without matching*.—The cross section obtained by applying the generator-level pre-selection cuts listed in Eq. (6);

(ii) $\sigma_{\textbf{xqcut}}$ *without matching*.—The cross section obtained by varying **xqcut**. The variation of **xqcut**

[17]In this appendix, we use the term of "parton" instead of "jet" to make a distinction from a clustered jet obtained by collecting several hard and soft partons.

TABLE XIII. Cut flow table of the backgrounds in terms of efficiencies (%) at the HL-LHC.

	Single-Higgs BG				Nonresonant BG				
Cuts	ggH	$t\bar{t}H$	ZH	$b\bar{b}H$	$b\bar{b}\gamma\gamma$	$c\bar{c}\gamma\gamma$	$jj\gamma\gamma$	$b\bar{b}j\gamma$	$c\bar{c}j\gamma$
1. Diphoton trigger	18.36	23.37	18.22	17.27	17.86	16.81	0.22	1.43×10^{-2}	0.02
2. ≥2 isolated photons	7.43	21.43	11.87	2.88	12.16	11.53	0.15	8.43×10^{-3}	0.01
3-1. Jet candidates	1.97	20.33	5.49	0.25	7.33	6.82	0.09	7.75×10^{-3}	0.01
3-2 ≥2 two b jets	1.99×10^{-2}	6.57	0.36	6.71×10^{-2}	2.13	0.24	2.60×10^{-3}	1.33×10^{-3}	1.98×10^{-4}
4. No. of jets ≤5	1.94×10^{-2}	5.16	0.36	6.70×10^{-2}	2.08	0.23	2.48×10^{-3}	1.23×10^{-3}	1.75×10^{-4}
5. Lepton veto	1.91×10^{-2}	3.85	0.36	6.66×10^{-2}	2.07	0.23	2.42×10^{-3}	1.23×10^{-3}	1.71×10^{-4}
6. $\Delta R_{\gamma\gamma,bb}$ cut	1.13×10^{-2}	1.16	0.26	1.73×10^{-2}	0.41	0.03	7.71×10^{-4}	2.93×10^{-4}	3.29×10^{-5}
7-1. Higgs mass window $M_{\gamma\gamma}$	1.08×10^{-2}	1.09	0.25	1.71×10^{-2}	1.85×10^{-2}	1.08×10^{-3}	3.56×10^{-5}	8.30×10^{-6}	9.35×10^{-7}
7-2. Higgs mass window M_{bb}	1.92×10^{-3}	0.37	5.39×10^{-2}	4.20×10^{-3}	4.85×10^{-3}	2.20×10^{-4}	1.14×10^{-5}	2.33×10^{-6}	2.65×10^{-7}
8. $p_{T_{\gamma\gamma}}$, $p_{T_{bb}}$	1.83×10^{-3}	0.32	5.38×10^{-2}	3.90×10^{-3}	4.49×10^{-3}	2.10×10^{-4}	6.88×10^{-6}	1.71×10^{-6}	1.75×10^{-7}
Other/barrel ratio	46.6%	34.5%	48.3%	39.6%	69.1%	57.2%	110.0%	80.4%	40.1%

	Nonresonant BG		$t\bar{t}$-related BG	
Cuts	$b\bar{b}jj$	$Z(b\bar{b})\gamma\gamma$	$t\bar{t}$	$t\bar{t}\gamma$
1. Diphoton trigger	7.33×10^{-6}	18.70	21.25	6.00
2. ≥2 isolated photons	3.90×10^{-7}	13.01	9.97	4.77
3-1. Jet candidates	3.90×10^{-7}	6.11	8.86	4.18
3-2. ≥2 two b jets	4.01×10^{-7}	1.24	2.23	1.21
4. No. of jets ≤5	2.85×10^{-7}	1.22	2.07	1.09
5. Lepton veto	2.80×10^{-7}	1.21	2.07	1.09
6. $\Delta R_{\gamma\gamma,bb}$ cut	8.76×10^{-8}	0.58	0.37	0.18
7-1. Higgs mass window $M_{\gamma\gamma}$	2.77×10^{-9}	2.64×10^{-2}	0.01	5.86×10^{-3}
7-2. Higgs mass window M_{bb}	6.98×10^{-10}	5.89×10^{-3}	3.79×10^{-3}	1.98×10^{-3}
8. $p_{T_{\gamma\gamma}}$, $p_{T_{bb}}$	4.25×10^{-10}	5.80×10^{-3}	2.40×10^{-3}	1.74×10^{-3}
Other/barrel ratio	45.4%	66.6%	63.8%	57.6%

TABLE XIV. Cut flow table of the backgrounds in terms of efficiencies (%) at the HL-100 TeV hadron collider.

	Single-Higgs BG				Nonresonant BG				
Cuts	ggH	$t\bar{t}H$	ZH	$b\bar{b}H$	$b\bar{b}\gamma\gamma$	$c\bar{c}\gamma\gamma$	$jj\gamma\gamma$	$b\bar{b}j\gamma$	$c\bar{c}j\gamma$
1. Diphoton trigger	60.04	45.79	54.04	64.18	44.55	44.13	0.33	0.08	7.58×10^{-2}
2. ≥ 2 isolated photons	22.87	31.53	22.91	11.97	15.44	16.85	0.09	0.03	2.73×10^{-2}
3-1. Jet candidates	8.85	30.71	11.31	1.22	10.52	12.02	0.06	0.03	2.56×10^{-2}
3-2. ≥ 2 two b jets	0.14	11.59	0.81	0.36	3.14	0.19	1.52×10^{-3}	0.01	4.19×10^{-4}
4. No. of jets ≤ 5	0.11	7.10	0.78	0.35	2.78	0.14	1.13×10^{-3}	4.35×10^{-3}	2.18×10^{-4}
5. Lepton veto	0.11	5.20	0.78	0.35	2.78	0.14	1.13×10^{-3}	4.35×10^{-3}	2.18×10^{-4}
6. $\Delta R_{\gamma\gamma,bb}$ cut	0.10	3.79	0.71	0.19	1.62	0.08	7.78×10^{-4}	2.30×10^{-3}	1.03×10^{-4}
7-1. Higgs mass window $M_{\gamma\gamma}$	0.09	3.45	0.67	0.18	0.07	3.35×10^{-3}	3.23×10^{-5}	6.38×10^{-5}	3.29×10^{-6}
7-2. Higgs mass window M_{bb}	0.02	0.97	0.33	0.04	0.02	9.45×10^{-4}	8.20×10^{-6}	2.07×10^{-5}	1.08×10^{-6}
8. $p_{T_{\gamma\gamma}}$, $p_{T_{bb}}$	0.02	0.40	0.22	0.02	5.21×10^{-3}	1.64×10^{-4}	2.00×10^{-6}	4.23×10^{-6}	2.33×10^{-7}
Other/barrel ratio	19.9%	31.8%	37.4%	40.3%	49.6%	100.0%	53.8%	42.0%	35.7%

	Nonresonant BG		$t\bar{t}$-related BG	
Cuts	$b\bar{b}jj$	$Z(b\bar{b})\gamma\gamma$	$t\bar{t}$	$t\bar{t}\gamma$
1. Diphoton trigger	1.33×10^{-4}	45.38	14.61	10.49
2. ≥2 isolated photons	5.77×10^{-5}	14.85	5.98	5.62
3-1. Jet candidates	5.77×10^{-5}	9.28	5.85	5.39

(Table continued)

TABLE XIV. *(Continued)*

	Nonresonant BG		$t\bar{t}$-related BG	
Cuts	$b\bar{b}jj$	$Z(b\bar{b})\gamma\gamma$	$t\bar{t}$	$t\bar{t}\gamma$
3-2. $\geq$2 two b jets	1.01×10^{-5}	2.06	1.81	1.88
4. No. of jets ≤ 5	5.41×10^{-6}	1.92	1.28	1.32
5. Lepton veto	5.41×10^{-6}	1.92	1.28	1.32
6. $\Delta R_{\gamma\gamma,bb}$ cut	3.17×10^{-6}	1.68	0.75	0.75
7-1. Higgs mass window $M_{\gamma\gamma}$	8.44×10^{-8}	0.07	0.02	0.02
7-2. Higgs mass window M_{bb}	2.79×10^{-8}	0.04	0.01	0.01
8. $p_{T_{\gamma\gamma}}$, $p_{T_{bb}}$	7.44×10^{-9}	0.02	1.31×10^{-3}	1.95×10^{-3}
Other/barrel ratio	55.6%	53.6%	54.8%	69.0%

TABLE XV. HL-LHC: The cross sections for the nonresonant backgrounds taking the PDF set of CT14LO. For the three merged cross sections, $Q_{\rm cut}/{\rm GeV} = 30$ (upper), 45 (middle), and 60 (low) are taken with the parameter **xqcut** set to 20 GeV.

Cross section	$b\bar{b}\gamma\gamma$	$c\bar{c}\gamma\gamma$	$jj\gamma\gamma$	$b\bar{b}j\gamma$	$c\bar{c}j\gamma$	$b\bar{b}jj$	$Z(b\bar{b})\gamma\gamma$
$\sigma_{\rm Eq.(6)}$ [fb]	112	1081	1.40×10^4	2.72×10^5	0.91×10^6	3.00×10^8	5.03
$\sigma_{\rm merged}$ [fb]	82.5	647	0.59×10^4	1.22×10^5	0.35×10^6	0.67×10^8	3.65
	82.3	662	0.44×10^4	0.96×10^5	0.25×10^6	0.28×10^8	3.68
	81.5	662	0.34×10^4	0.78×10^5	0.18×10^6	0.13×10^8	3.68
$\delta\sigma/\sigma$ [%]	1.2	2.3	42	36	49	81	0.8

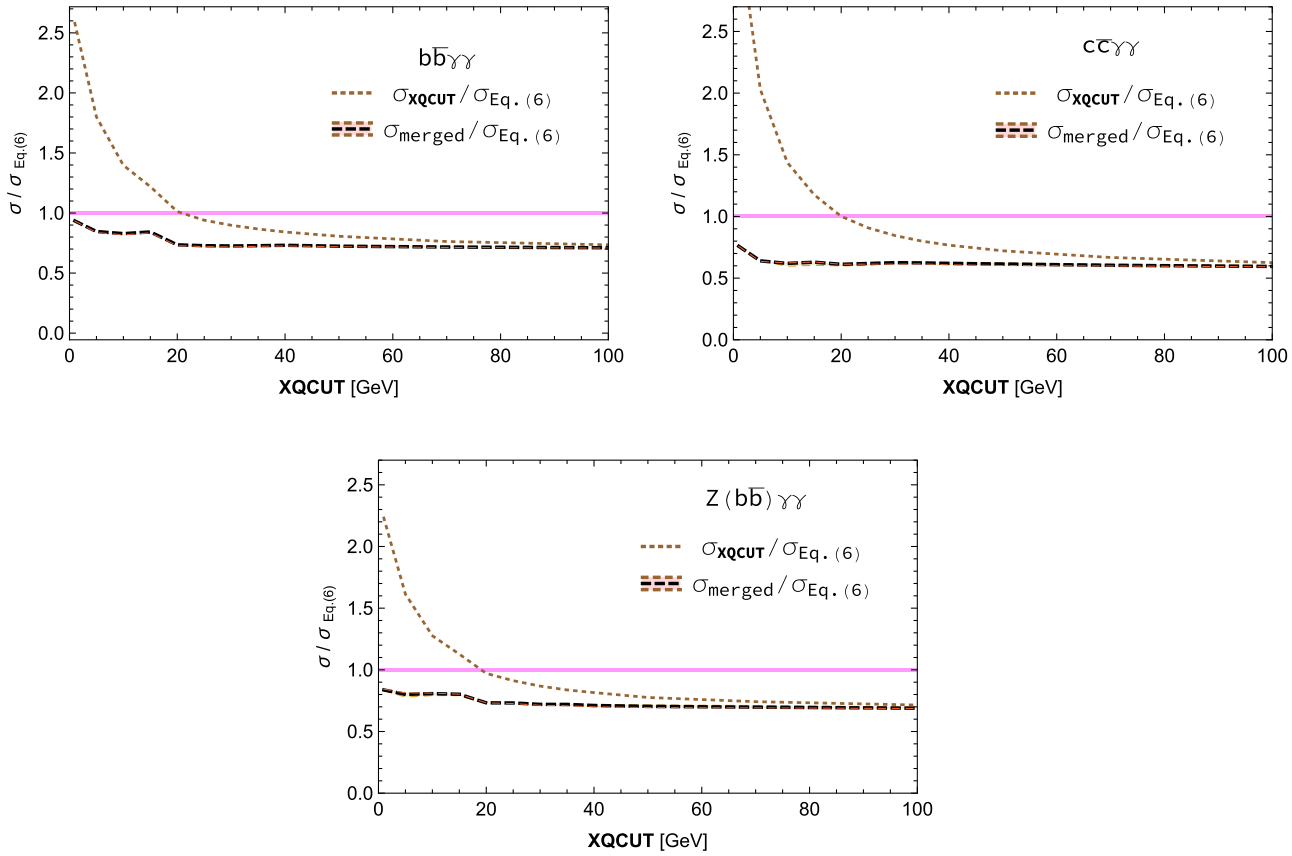

FIG. 16. The dependence of the ratios of $\sigma_{\mathbf{xqcut}}/\sigma_{\rm Eq.(6)}$ (dotted lines) and $\sigma_{\rm merged}/\sigma_{\rm Eq.(6)}$ (bands) on **xqcut** for the nonresonant backgrounds of $b\bar{b}\gamma\gamma$ (upper left), $c\bar{c}\gamma\gamma$ (upper right), and $Z(b\bar{b})\gamma\gamma$ (lower). The horizontal magenta lines locate the positions where $\sigma_{\mathbf{xqcut}} = \sigma_{\rm Eq.(6)}$. The bands show the variation of the merged cross sections depending on the choice of $Q_{\rm cut}/\mathbf{xqcut}$: 1.5, 3 (upper and lower boundaries), and 2.25 (middle dashed line). The bandwidth for all three processes is negligible.

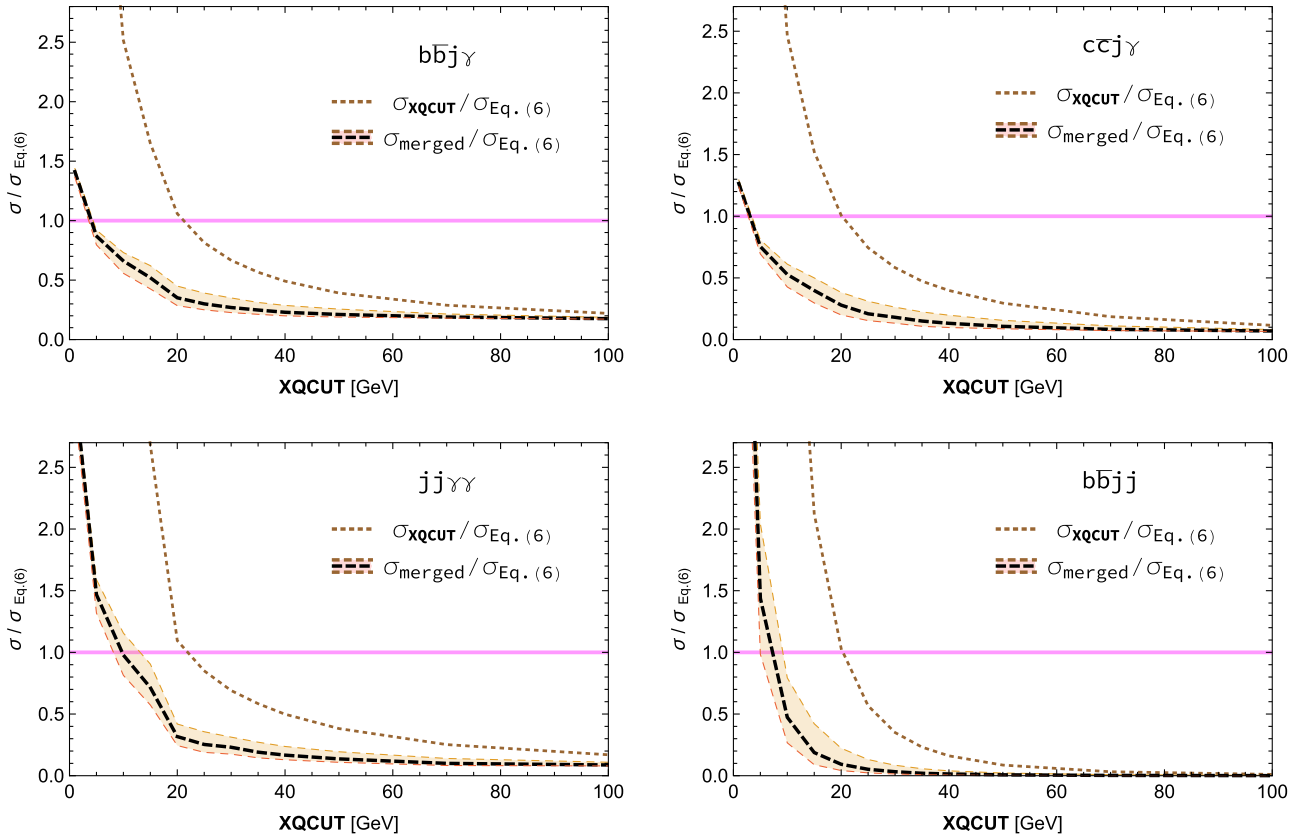

FIG. 17. The same as in Fig. 16 but for the nonresonant backgrounds of $b\bar{b}j\gamma$ (upper left), $c\bar{c}j\gamma$ (upper right), $jj\gamma\gamma$ (lower left), and $b\bar{b}jj$ (lower right).

affects the preselection cuts on P_{T_j}, M_{jj}, and ΔR_{jj}. Otherwise, the other preselection cuts remain the same as in Eq. (6).

(iii) σ_{merged} *with MLM matching.*—The cross section obtained after implementing MLM matching. The merged cross section depends on the parameters of **xqcut** and Q_{cut}. In the default MG5_aMC@NLO setting, when a value of **xqcut** is given, three merged cross sections are provided for the three values of $Q_{\mathrm{cut}}/\mathbf{xqcut}$: 1.5, 2.25, and 3. For the representative value, the merged cross section with $Q_{\mathrm{cut}}/\mathbf{xqcut} = 1.5$ is taken.

For further discussion, it is helpful to introduce the distance between the two objects (d_{ij}) and that between an object and the beam direction (d_{iB}). Here an object could stand for a hard parton at the matrix-element level, a showering soft parton, or a clustered jet. Precisely,

$$d_{ij} = \min(P_{T_i}^{2p}, P_{T_j}^{2p})\frac{\Delta R_{ij}^2}{R^2}, \qquad d_{iB} = P_{T_i}^{2p}, \quad \text{(C1)}$$

where the parameter R defines the jet size and the parameter p the jet algorithm used. In MLM matching, the k_T algorithm with $p = 1$ is used. We note that $\sqrt{d_{iB}}$ in the k_T algorithm is nothing but P_{T_i} or the transverse momentum of an object.

Roughly speaking, the calculation of the merged cross section proceeds as the following steps:

(i) generation of hard partons with $\sqrt{d_{ij}}, \sqrt{d_{iB}} >$ **xqcut** at the matrix-element level,

(ii) showering soft partons with $\sqrt{d_{ij}}, \sqrt{d_{iB}} < \mu_F$ with μ_F being the factorization scale,

(iii) clustering partons and pseudopartons into jets according to a certain jet algorithm until all the distances among clustered jets and the beam direction are smaller than Q_{cut}^2,

(iv) matching by requiring that the number of jets obtained at step (iii) should be equal to the number of hard partons at step (i),[18] and the distance between a jet and its nearest hard parton is smaller than $\max\{Q_{\mathrm{cut}}^2, P_T^2\}$ with P_T being the transverse momentum of the nearest hard parton, and

(v) calculating the merged cross section by exploiting the weight factors and other information obtained in the matching step (iv).

[18]Sometimes, for the highest multiplicity sample, the number of jets is required to be equal to or larger than the number of hard partons.

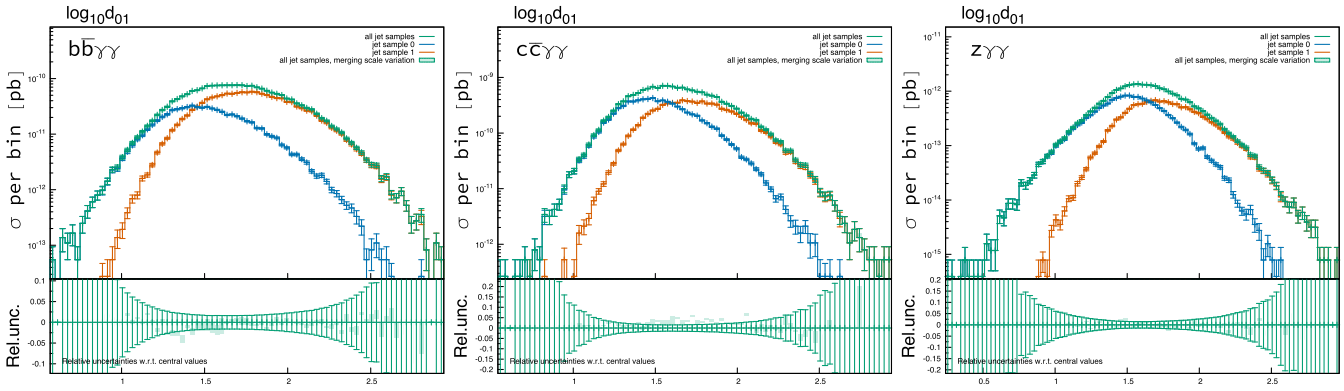

FIG. 18. HL-LHC: The differential jet rate (DJR) distributions for the nonresonant backgrounds of $b\bar{b}\gamma\gamma$ (left), $c\bar{c}\gamma\gamma$ (middle), and $Z(b\bar{b})\gamma\gamma$ (right) taking **xqcut** $= 20$ GeV and $Q_{\rm cut} = 30$ GeV. Here, "jet sample 0" and "jet sample 1" refer to the samples containing 0 and 1 hard parton, respectively, with $\sqrt{d_{ij}}, \sqrt{d_{iB}} >$ **xqcut** at the matrix-element level.

In Table XV, we present the cross sections of $\sigma_{\rm Eq.\,(6)}\sigma_{\rm Eq.\,(6)}$ and $\sigma_{\rm merged}$. For the three merged cross sections, $Q_{\rm cut}/{\rm GeV} = 30$ (upper), 45 (middle), and 60 (low) are taken with the parameter **xqcut** set to 20 GeV. Note that the smaller value of $Q_{\rm cut}$ usually results in the larger $\sigma_{\rm merged}$. First of all, we observe that $\sigma_{\rm Eq.\,(6)}$'s are smaller than those presented in Table I. This is because the PDF set of CT14LO is taken for this table, while, in Table I, the PDF set of CTEQ6L1 is taken. The difference between $\sigma_{\rm Eq.(6)}$ and $\sigma_{\rm merged}$ could be interpreted as the degree of double counting. Furthermore, the variation of the merged cross sections depending on the choice of $Q_{\rm cut}$ may provide

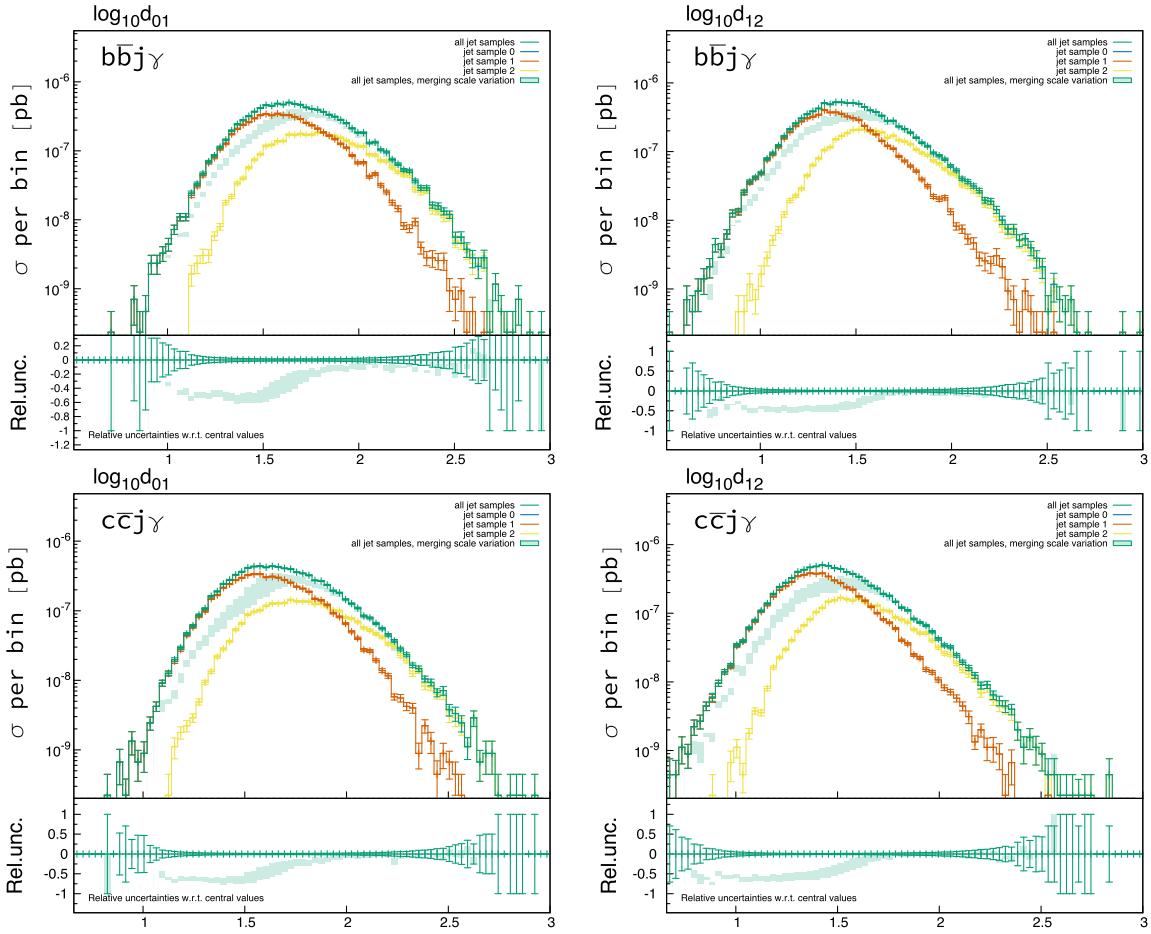

FIG. 19. HL-LHC: The DJR distributions for the nonresonant backgrounds of $b\bar{b}j\gamma$ (upper) and $c\bar{c}j\gamma$ (lower) taking **xqcut** $= 20$ GeV and $Q_{\rm cut} = 30$ GeV. Here, "jet sample n" refers to the sample containing n hard partons at the matrix-element level.

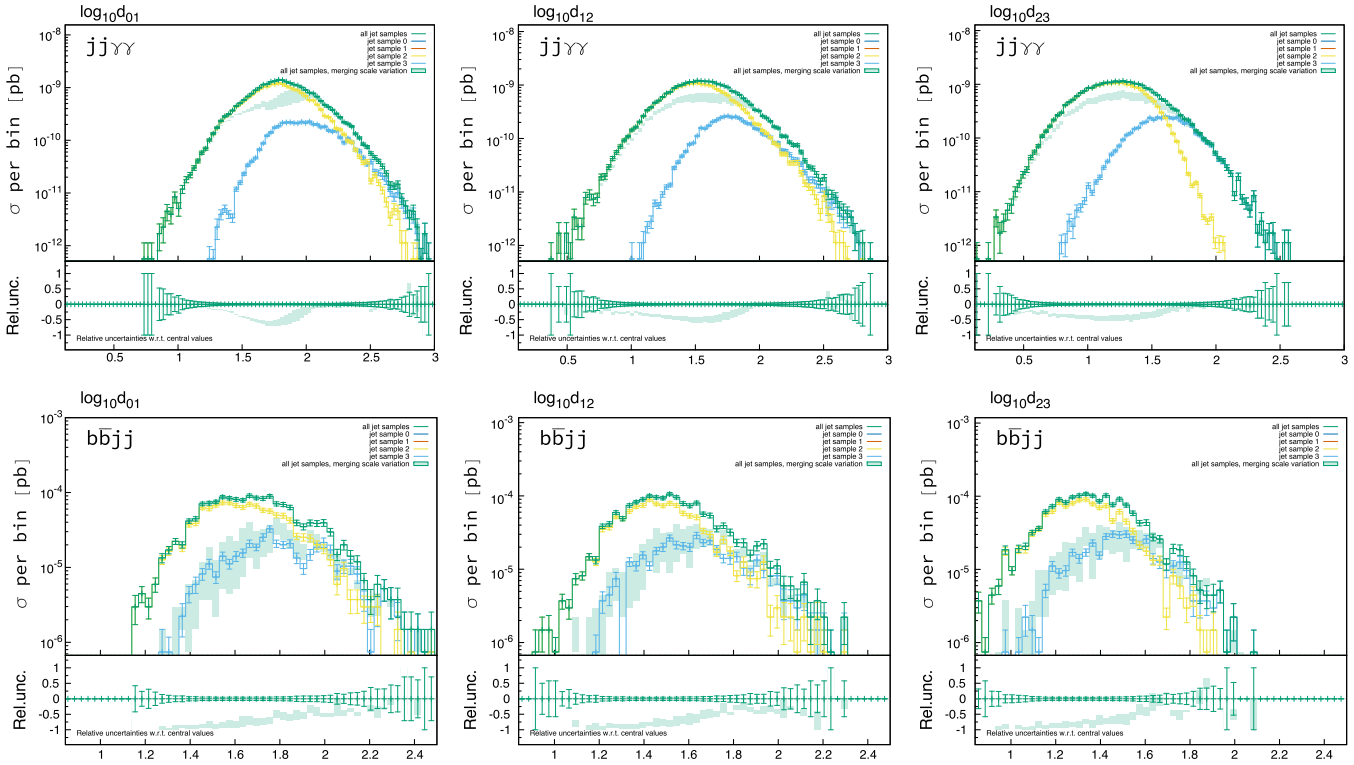

FIG. 20. HL-LHC: The DJR distributions for the nonresonant backgrounds of $jj\gamma\gamma$ (upper) and $b\bar{b}jj$ (lower) taking $\mathbf{xqcut} = 20$ GeV and $Q_{\rm cut} = 30$ GeV. Here, jet sample n refers to the sample containing n hard partons at the matrix-element level.

a measure of the quality of the matching. For quantitative estimation of the matching quality, we introduce the following quantity:

$$\frac{\delta\sigma}{\sigma} \equiv \frac{|\sigma^{Q_{\rm cut}/{\rm xqcut}=1.5}_{\rm merged} - \sigma^{Q_{\rm cut}/{\rm xqcut}=3}_{\rm merged}|}{\sigma^{Q_{\rm cut}/{\rm xqcut}=1.5}_{\rm merged}}.$$

We observe $\delta\sigma/\sigma$ is less than about 2% for $b\bar{b}\gamma\gamma$, $c\bar{c}\gamma\gamma$, and $Z(b\bar{b})\gamma\gamma$, and it is about 40% for $b\bar{b}j\gamma$, $c\bar{c}j\gamma$, and $jj\gamma\gamma$. For $b\bar{b}jj$, on the other hand, it amounts to more than 80%.

Figure 16 shows the ratios of $\sigma_{\mathbf{xqcut}}/\sigma_{\rm Eq.\,(6)}$ and $\sigma_{\rm merged}/\sigma_{\rm Eq.\,(6)}$ as functions of **xqcut** for the nonresonant backgrounds of $b\bar{b}\gamma\gamma$ (upper left), $c\bar{c}\gamma\gamma$ (upper right), and $Z(b\bar{b})\gamma\gamma$ (lower). In each frame, the dotted curve is for $\sigma_{\mathbf{xqcut}}/\sigma_{\rm Eq.\,(6)}$, and the band with a dashed line at its center for $\sigma_{\rm merged}/\sigma_{\rm Eq.\,(6)}$. A band is delimited by the choices of $Q_{\rm cut}/\mathbf{xqcut} = 1.5$ and 3, while the center line is obtained by taking $Q_{\rm cut}/\mathbf{xqcut} = 2.25$. For a given value of **xqcut**, the larger value of $Q_{\rm cut}$ usually leads to the smaller merged cross section. First of all, we observe that $\sigma_{\mathbf{xqcut}} = \sigma_{\rm Eq.\,(6)}$ around $\mathbf{xqcut} \simeq 20$ GeV, which is nothing but the value of P_{T_j} cut; see Eq. (6). $\sigma_{\rm merged}$ is always smaller than $\sigma_{\mathbf{xqcut}}$, and the difference between them could be interpreted as the degree of double counting. We note that the difference becomes smaller when **xqcut** grows. This is because the leading process without an additional hard parton dominates more and more as the value of **xqcut** becomes large.

For the choice of $Q_{\rm cut}/\mathbf{xqcut} = 1.5$ and $\mathbf{xqcut} = 20$ GeV, compared to $\sigma_{\mathbf{xqcut}}$, the merged cross sections for $b\bar{b}\gamma\gamma$, $c\bar{c}\gamma\gamma$, and $Z(b\bar{b})\gamma\gamma$ decrease by about 30%. Incidentally, we note the bandwidths are negligible for $b\bar{b}\gamma\gamma$, $c\bar{c}\gamma\gamma$, and $Z(b\bar{b})\gamma\gamma$.

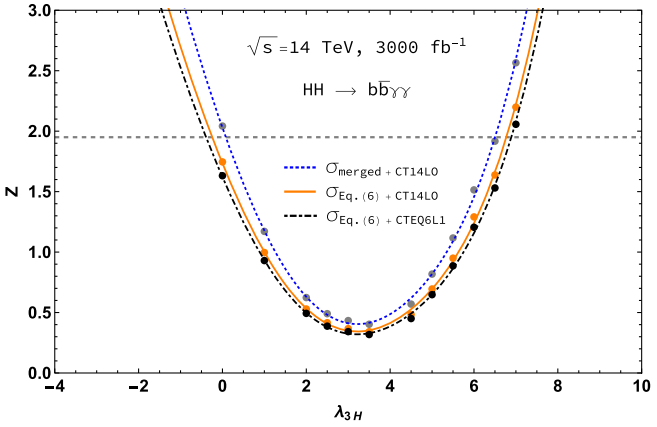

FIG. 21. HL-LHC: Significance of the signal over the background versus λ_{3H} taking $\sigma_{\rm Eq.\,(6)}$ (red solid line) and $\sigma_{\rm merged}$ (blue dashed line) for the nonresonant backgrounds. The PDF set of CT14LO is taken. For comparison, also shown is the case with the PDF set of CTEQ6L1 (black dash-dotted line). Note that the NNLO cross section $\sigma(gg \to HH) = 36.69$ fb in the FT approximation is taken and the λ_{3H}-dependent QCD corrections have been included; see Fig. 12.

Figure 17 shows the ratios of $\sigma_{\mathbf{xqcut}}/\sigma_{\mathrm{Eq.(6)}}$ and $\sigma_{\mathrm{merged}}/\sigma_{\mathrm{Eq.(6)}}$ as functions of **xqcut** for the nonresonant backgrounds of $b\bar{b}j\gamma$ (upper left), $c\bar{c}j\gamma$ (upper right), $jj\gamma\gamma$ (lower left), and $b\bar{b}jj$ (lower right). Compared to $b\bar{b}\gamma\gamma$, $c\bar{c}\gamma\gamma$, and $Z(b\bar{b})\gamma\gamma$ in Fig. 16, the reduction of the merged cross sections is larger and the bandwidth is sizable.

Figures 18–20 show the differential jet rate (DJR) distributions after hadronization, multiparton interactions (MPI), and decays for all the nonresonant backgrounds taking $\mathbf{xqcut} = 20$ GeV and $Q_{\mathrm{cut}} = 30$ GeV. We observe that the DJR distributions for $b\bar{b}\gamma\gamma$, $c\bar{c}\gamma\gamma$, and $Z(b\bar{b})\gamma\gamma$ are very smooth, and the variation of the merged cross sections depending on the choice of Q_{cut} is negligible. For $b\bar{b}j\gamma$, $c\bar{c}j\gamma$, and $jj\gamma\gamma$, the distributions are smooth and the variation is small. For $b\bar{b}jj$, the DJR distributions are coarse and the variation of the merged cross section is sizable.

In conclusion, the matching has been excellently implemented for $b\bar{b}\gamma\gamma$, $c\bar{c}\gamma\gamma$, and $Z(b\bar{b})\gamma\gamma$ backgrounds, and it is less successful for $jj\gamma\gamma$, $b\bar{b}j\gamma$, and $c\bar{c}j\gamma$. On the other hand, for $b\bar{b}jj$, it is doubtful whether the merged cross section is trustworthy. Therefore, for $b\bar{b}\gamma\gamma$, $c\bar{c}\gamma\gamma$, and $Z(b\bar{b})\gamma\gamma$, one may safely use the merged cross sections obtained by matching the leading and subleading processes. For $jj\gamma\gamma$, $b\bar{b}j\gamma$, and $c\bar{c}j\gamma$, they are less reliable. And, for $b\bar{b}jj$, it might be recommended to use $\sigma_{\mathrm{Eq.(6)}}$ for conservative estimation of the background.

To see the impact of matching for the nonresonant backgrounds, we show the significance of the signal over the background versus λ_{3H} in Fig. 21. We find that the 95% C.L. region is reduced by the amount of about 15% taking the merged cross sections for the nonresonant backgrounds with CT14LO.

[1] P. W. Higgs, Phys. Rev. Lett. **13**, 508 (1964); F. Englert and R. Brout, Phys. Rev. Lett. **13**, 321 (1964); G. S. Guralnik, C. R. Hagen, and T. W. B. Kibble, Phys. Rev. Lett. **13**, 585 (1964).

[2] G. Aad *et al.* (ATLAS Collaboration), Phys. Lett. B **716**, 1 (2012); S. Chatrchyan *et al.* (CMS Collaboration), Phys. Lett. B **716**, 30 (2012).

[3] K. Cheung, J. S. Lee, and P. Y. Tseng, J. High Energy Phys. 05 (2013) 134; Phys. Rev. D **90**, 095009 (2014).

[4] E. W. N. Glover and J. J. van der Bij, Nucl. Phys. **B309**, 282 (1988); D. A. Dicus, C. Kao, and S. S. D. Willenbrock, Phys. Lett. B **203**, 457 (1988); T. Plehn, M. Spira, and P. M. Zerwas, Nucl. Phys. **B479**, 46 (1996); **B531**, 655(E) (1998); A. Djouadi, W. Kilian, M. Muhlleitner, and P. M. Zerwas, Eur. Phys. J. C **10**, 45 (1999); S. Dawson, S. Dittmaier, and M. Spira, Phys. Rev. D **58**, 115012 (1998); U. Baur, T. Plehn, and D. L. Rainwater, Phys. Rev. D **67**, 033003 (2003); T. Binoth, S. Karg, N. Kauer, and R. Ruckl, Phys. Rev. D **74**, 113008 (2006).

[5] U. Baur, T. Plehn, and D. L. Rainwater, Phys. Rev. D **68**, 033001 (2003); Phys. Rev. Lett. **89**, 151801 (2002); Phys. Rev. D **69**, 053004 (2004).

[6] J. Baglio, A. Djouadi, R. Grber, M. M. Mhlleitner, J. Quevillon, and M. Spira, J. High Energy Phys. 04 (2013) 151; J. Grigo, J. Hoff, K. Melnikov, and M. Steinhauser, Nucl. Phys. **B875**, 1 (2013); V. Barger, L. L. Everett, C. B. Jackson, and G. Shaughnessy, Phys. Lett. B **728**, 433 (2014); W. Yao, arXiv:1308.6302.

[7] C. Englert, F. Krauss, M. Spannowsky, and J. Thompson, Phys. Lett. B **743**, 93 (2015); T. Liu and H. Zhang, arXiv:1410.1855; D. E. Ferreira de Lima, A. Papaefstathiou, and M. Spannowsky, J. High Energy Phys. 08 (2014) 030; V. Barger, L. L. Everett, C. B. Jackson, and G. Shaughnessy, Phys. Lett. B **728**, 433 (2014); E. Asakawa, D. Harada, S. Kanemura, Y. Okada, and K. Tsumura, Phys. Rev. D **82**, 115002 (2010); A. Papaefstathiou, L. L. Yang, and J. Zurita, Phys. Rev. D **87**, 011301 (2013); A. Papaefstathiou, Phys. Rev. D **91**, 113016 (2015); R. Frederix, S. Frixione, V. Hirschi, F. Maltoni, O. Mattelaer, P. Torrielli, E. Vryonidou, and M. Zaro, Phys. Lett. B **732**, 142 (2014).

[8] K. Nishiwaki, S. Niyogi, and A. Shivaji, J. High Energy Phys. 04 (2014) 011; M. Gouzevitch, A. Oliveira, J. Rojo, R. Rosenfeld, G. P. Salam, and V. Sanz, J. High Energy Phys. 07 (2013) 148; M. J. Dolan, C. Englert, and M. Spannowsky, J. High Energy Phys. 10 (2012) 112; A. Azatov, R. Contino, G. Panico, and M. Son, Phys. Rev. D **92**, 035001 (2015); N. Liu, S. Hu, B. Yang, and J. Han, J. High Energy Phys. 01 (2015) 008; F. Goertz, A. Papaefstathiou, L. L. Yang, and J. Zurita, J. High Energy Phys. 04 (2015) 167; R. Grober, M. Muhlleitner, M. Spira, and J. Streicher, J. High Energy Phys. 09 (2015) 092; F. Goertz, A. Papaefstathiou, L. L. Yang, and J. Zurita, J. High Energy Phys. 06 (2013) 016; R. Contino, M. Ghezzi, M. Moretti, G. Panico, F. Piccinini, and A. Wulzer, J. High Energy Phys. 08 (2012) 154; C. R. Chen and I. Low, Phys. Rev. D **90**, 013018 (2014); R. S. Gupta, H. Rzehak, and J. D. Wells, Phys. Rev. D **88**, 055024 (2013); D. Goncalves, T. Han, F. Kling, T. Plehn, and M. Takeuchi, Phys. Rev. D **97**, 113004 (2018); Q. H. Cao, B. Yan, D. M. Zhang, and H. Zhang, Phys. Lett. B **752**, 285 (2016); Q. H. Cao, G. Li, B. Yan, D. M. Zhang, and H. Zhang, Phys. Rev. D **96**, 095031 (2017); H. J. He, J. Ren, and W. Yao, Phys. Rev. D **93**, 015003 (2016).

[9] S. Dawson, E. Furlan, and I. Lewis, Phys. Rev. D **87**, 014007 (2013); M. Gillioz, R. Grober, C. Grojean, M. Muhlleitner, and E. Salvioni, J. High Energy Phys. 10 (2012) 004; V. Barger, L. L. Everett, C. B. Jackson, A. Peterson, and G. Shaughnessy, Phys. Rev. Lett. **114**, 011801 (2015); M. J. Dolan, C. Englert, and M. Spannowsky, Phys. Rev. D **87**, 055002 (2013); G. D. Kribs and A. Martin, Phys. Rev. D **86**, 095023 (2012); A. Arhrib, R. Benbrik, C. H.

Chen, R. Guedes, and R. Santos, J. High Energy Phys. 08 (2009) 035; C. O. Dib, R. Rosenfeld, and A. Zerwekh, J. High Energy Phys. 05 (**2006**) 074; R. Grober and M. Muhlleitner, J. High Energy Phys. 06 (2011) 020; J. M. No and M. Ramsey-Musolf, Phys. Rev. D **89**, 095031 (2014); B. Hespel, D. Lopez-Val, and E. Vryonidou, J. High Energy Phys. 09 (2014) 124; S. M. Etesami and M. Mohammadi Najafabadi, Phys. Rev. D **92**, 073013 (2015); T. Corbett, A. Joglekar, H. L. Li, and J. H. Yu, J. High Energy Phys. 05 (2018) 061.

[10] C. Han, X. Ji, L. Wu, P. Wu, and J. M. Yang, J. High Energy Phys. 04 (2014) 003; U. Ellwanger, J. High Energy Phys. 08 (2013) 077; J. Cao, Z. Heng, L. Shang, P. Wan, and J. M. Yang, J. High Energy Phys. 04 (2013) 134; B. Bhattacherjee and A. Choudhury, Phys. Rev. D **91**, 073015 (2015); D. T. Nhung, M. Muhlleitner, J. Streicher, and K. Walz, J. High Energy Phys. 11 (2013) 181.

[11] C. T. Lu, J. Chang, K. Cheung, and J. S. Lee, J. High Energy Phys. 08 (2015) 133.

[12] A. J. Barr, M. J. Dolan, C. Englert, and M. Spannowsky, Phys. Lett. B **728**, 308 (2014); M. J. Dolan, C. Englert, N. Greiner, and M. Spannowsky, Phys. Rev. Lett. **112**, 101802 (2014); F. Bishara, R. Contino, and J. Rojo, Eur. Phys. J. C **77**, 481 (2017); M. J. Dolan, C. Englert, N. Greiner, K. Nordstrom, and M. Spannowsky, Eur. Phys. J. C **75**, 387 (2015); J. K. Behr, D. Bortoletto, J. A. Frost, N. P. Hartland, C. Issever, and J. Rojo, Eur. Phys. J. C **76**, 386 (2016); V. Martn Lozano, J. M. Moreno, and C. B. Park, J. High Energy Phys. 08 (2015) 004; Q. H. Cao, Y. Liu, and B. Yan, Phys. Rev. D **95**, 073006 (2017); S. Di Vita, C. Grojean, G. Panico, M. Riembau, and T. Vantalon, J. High Energy Phys. 09 (2017) 069; A. Adhikary, S. Banerjee, R. K. Barman, B. Bhattacherjee, and S. Niyogi, J. High Energy Phys. 07 (2018) 116; J. H. Kim, Y. Sakaki, and M. Son, Phys. Rev. D **98**, 015016 (2018).

[13] S. Homiller and P. Meade, J. High Energy Phys. 03 (2019) 055.

[14] See T. Plehn *et al.* in Ref. [4].

[15] D. de Florian and J. Mazzitelli, J. High Energy Phys. 09 (2015) 053.

[16] R. Frederix, S. Frixione, V. Hirschi, F. Maltoni, O. Mattelaer, P. Torrielli, E. Vryonidou, and M. Zaro, Phys. Lett. B **732**, 142 (2014).

[17] J. Baglio, A. Djouadi, R. Grber, M. M. Mhlleitner, J. Quevillon, and M. Spira, J. High Energy Phys. 04 (2013) 151.

[18] D. de Florian *et al.* (LHC Higgs Cross Section Working Group), https://doi.org/10.23731/CYRM-2017-002.

[19] Higgs Cross Section Working Group, https://cern.ch/twiki/bin/view/LHCPhysics/LHCHXSWG.

[20] R. Contino *et al.*, CERN Yellow Report No. 3, 255, https://doi.org/10.23731/CYRM-2017-003.255 (2017).

[21] M. Vos, arXiv:1701.06537.

[22] M. Czakon and A. Mitov, Comput. Phys. Commun. **185**, 2930 (2014).

[23] K. Melnikov, M. Schulze, and A. Scharf, Phys. Rev. D **83**, 074013 (2011).

[24] J. Alwall, R. Frederix, S. Frixione, V. Hirschi, F. Maltoni, O. Mattelaer, H.-S. Shao, T. Stelzer, P. Torrielli, and M. Zaro, J. High Energy Phys. 07 (**2014**) 079.

[25] P. Nason, J. High Energy Phys. 11 (2004) 040; S. Frixione, P. Nason, and C. Oleari, J. High Energy Phys. 11 (2007) 070; S. Alioli, P. Nason, C. Oleari, and E. Re, J. High Energy Phys. 06 (2010) 043.

[26] T. Sjstrand, S. Ask, J. R. Christiansen, R. Corke, N. Desai, P. Ilten, S. Mrenna, S. Prestel, C. O. Rasmussen, and P. Z. Skands, Comput. Phys. Commun. **191**, 159 (2015).

[27] C. Degrande, C. Duhr, B. Fuks, D. Grellscheid, O. Mattelaer, and T. Reiter, Comput. Phys. Commun. **183**, 1201 (2012).

[28] V. Hirschi and O. Mattelaer, J. High Energy Phys. 10 (2015) 146.

[29] P. Artoisenet, R. Frederix, O. Mattelaer, and R. Rietkerk, J. High Energy Phys. 03 (**2013**) 015.

[30] ATLAS Collaboration, CERN Report No. ATL-PHYS-PUB-2017-001, 2017, http://cds.cern.ch/record/2243387.

[31] J. de Favereau, C. Delaere, P. Demin, A. Giammanco, V. Lemaître, A. Mertens, and M. Selvaggi (DELPHES 3 Collaboration), J. High Energy Phys. 02 (2014) 057.

[32] ATLAS Collaboration, CERN Report No. ATL-PHYS-PUB-2016-026, 2016, http://cds.cern.ch/record/2223839.

[33] ATLAS Collaboration, CERN Report No. ATL-PHYS-PUB-2015-022, 2015.

[34] R. D. Ball *et al.* (NNPDF Collaboration), J. High Energy Phys. 04 (2015) 040.

[35] J. Pumplin, D. R. Stump, J. Huston, H. L. Lai, P. M. Nadolsky, and W. K. Tung, J. High Energy Phys. 07 (2002) 012.

[36] H. L. Lai, M. Guzzi, J. Huston, Z. Li, P. M. Nadolsky, J. Pumplin, and C.-P. Yuan, Phys. Rev. D **82**, 074024 (2010).

[37] ATLAS Collaboration, CERN Report No. ATLAS-CONF-2014-046, 2014.

[38] https://twiki.cern.ch/twiki/bin/view/LHCPhysics/HiggsEuropeanStrategy.

[39] A. J. Barr, M. J. Dolan, C. Englert, D. E. Ferreira de Lima, and M. Spannowsky, J. High Energy Phys. 02 (2015) 016.

[40] F. Kling, T. Plehn, and P. Schichtel, Phys. Rev. D **95**, 035026 (2017).

[41] S. Borowka, N. Greiner, G. Heinrich, S. P. Jones, M. Kerner, J. Schlenk, U. Schubert, and T. Zirke, Phys. Rev. Lett. **117**, 012001 (2016); **117**, 079901(E) (2016).

[42] S. Borowka, N. Greiner, G. Heinrich, S. P. Jones, M. Kerner, J. Schlenk, and T. Zirke, J. High Energy Phys. 10 (2016) 107.

[43] M. Grazzini, G. Heinrich, S. Jones, S. Kallweit, M. Kerner, J. M. Lindert, and J. Mazzitelli, J. High Energy Phys. 05 (2018) 059.

[44] F. Maltoni, E. Vryonidou, and M. Zaro, J. High Energy Phys. 11 (2014) 079.

[45] S. Dulat, T.-J. Hou, J. Gao, M. Guzzi, J. Huston, P. Nadolsky, J. Pumplin, C. Schmidt, D. Stump, and C.-P. Yuan, Phys. Rev. D **93**, 033006 (2016).

[46] M. L. Mangano, M. Moretti, F. Piccinini, and M. Treccani, J. High Energy Phys. 01 (2007) 013.

[47] J. Alwall *et al.*, Eur. Phys. J. C **53**, 473 (2008).